


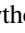











Abundances in the Milky Way across Five Nucleosynthetic Channels from 4 Million LAMOST Stars

Adam Wheeler¹ , Melissa Ness^{1,2} , Sven Buder^{3,4,5} , Joss Bland-Hawthorn^{5,6} , Gayandhi De Silva⁷, Michael Hayden^{5,6} , Janez Kos⁸, Geraint F. Lewis⁶ , Sarah Martell^{5,9} , Sanjib Sharma^{5,6} , Jeffrey D. Simpson⁹ , D. B. Zucker^{10,11} , and Tomaž Zwitter⁸ 

¹ Department of Astronomy, Columbia University, Pupin Physics Laboratories, New York, NY 10027, USA; a.wheeler@columbia.edu

² Center for Computational Astrophysics, Flatiron Institute, 162 Fifth Avenue, New York, NY 10010, USA

³ Max Planck Institute for Astronomy (MPIA), Königstuhl 17, D-69117 Heidelberg, Germany

⁴ Research School of Astronomy & Astrophysics, Australian National University, Canberra, ACT 2611, Australia

⁵ ARC Centre of Excellence for All Sky Astrophysics in 3 Dimensions (ASTRO 3D), Canberra, ACT 2611, Australia

⁶ Sydney Institute for Astronomy, School of Physics, A28, The University of Sydney, NSW 2006, Australia

⁷ Australian Astronomical Optics, Macquarie University, 105 Delhi Road, North Ryde, NSW 2113, Australia

⁸ University of Ljubljana, Faculty of Mathematics and Physics, Jadranska 19, 1000 Ljubljana, Slovenia

⁹ School of Physics, UNSW, Sydney, NSW 2052, Australia

¹⁰ Department of Physics and Astronomy, WW7 2.705, Macquarie University, NSW 2109 Australia

¹¹ Macquarie University Research Centre for Astronomy, Astrophysics & Astrophotonics, Sydney, NSW 2109, Australia

Received 2019 December 26; revised 2020 May 14; accepted 2020 June 6; published 2020 July 23

Abstract

Large stellar surveys are revealing the chemodynamical structure of the Galaxy across a vast spatial extent. However, the many millions of low-resolution spectra observed to date are yet to be fully exploited. We employ *The Cannon*, a data-driven approach for estimating chemical abundances, to obtain detailed abundances from low-resolution ($R = 1800$) LAMOST spectra, using the GALAH survey as our reference. We deliver five (for dwarfs) or six (for giants) estimated abundances representing five different nucleosynthetic channels, for 3.9 million stars, to a precision of 0.05–0.23 dex. Using wide binary pairs, we demonstrate that our abundance estimates provide chemical discriminating power beyond metallicity alone. We show the coverage of our catalog with radial, azimuthal and dynamical abundance maps and examine the neutron capture abundances across the disk and halo, which indicate different origins for the in situ and accreted halo populations. LAMOST has near-complete Gaia coverage and provides an unprecedented perspective on chemistry across the Milky Way.

Unified Astronomy Thesaurus concepts: [Chemical abundances \(224\)](#); [Milky Way Galaxy \(1054\)](#)

1. Introduction

Large stellar surveys such as Gaia (Gaia Collaboration et al. 2016), APOGEE (García Pérez et al. 2016; Majewski et al. 2017; Holtzman et al. 2018), GALAH (De Silva et al. 2015; Martell et al. 2017), Gaia-ESO (Gilmore et al. 2012), RAVE (Steinmetz et al. 2006), LAMOST (Newberg et al. 2012; Zhao et al. 2012) and SEGUE (Yanny et al. 2009) are providing the data to empirically characterize the Milky Way disk and infer the primary drivers of its formation and evolution (Freeman & Bland-Hawthorn 2002; Bland-Hawthorn & Gerhard 2016).

Detailed chemical abundances are one of the primary measurements made from stellar spectra. Their determination is a primary motivation for medium- and high-resolution spectroscopic surveys for several reasons: they provide effective chemical fingerprints of stars, link directly to the environment in which they were born (e.g., Krumholz et al. 2019), and describe the chemical diversity of the disk (e.g., Weinberg et al. 2019) and the chemical pathways of enrichment (e.g., Rybizki et al. 2017). Combined with stellar kinematics, abundances are core to the pursuit of Galactic archeology.

Conventionally, detailed abundances have been derived from medium- and high-resolution stellar spectra (e.g., APOGEE: $R = 22,500$; GALAH: $R = 28,000$; RAVE: $R = 7500$; Gaia-ESO: at least $R = 20,000$) Until recently, the inferences from low-resolution spectra, such as LAMOST and SEGUE, were typically limited to stellar parameters and α -enhancements (T_{eff} , $\log(g)$, $[\text{Fe}/\text{H}]$, $[\alpha/\text{Fe}]$) (e.g., Lee et al. 2011). Ting et al. (2018a) have shown that oxygen abundances can be inferred from spectra

in wavelength regions containing no atomic oxygen lines through the features of species in the CNO atomic-molecular network. Indirectly inferred abundances also have a long empirical history. The Ca II triplet, for example, is an often-used metallicity index (Armandroff & Zinn 1988; see Vásquez et al. 2015 for a recent calibration). To date, with the exception of Xiang et al. (2019), the efforts to extract individual abundances from LAMOST have largely focused on a few elements, namely, an integrated α -element abundance and the elements C and N, which are particularly important, as these elements can indicate age (e.g., Li et al. 2016; Ho et al. 2017a, 2017b; Xiang et al. 2017; Zhang et al. 2019).

In this work, we use a data-driven approach to label low-resolution LAMOST spectra with several abundances. LAMOST is one of the largest stellar surveys to date, with over 5×10^6 publicly available spectra, at $R = 1800$. The survey has extensive coverage of the Milky Way’s disk, halo, and, in particular, the outer disk, the detailed chemodynamics of which are largely unexplored. Specifically, we employ *The Cannon* (Ness et al. 2015), a model characterized in large part by its simplicity, to derive individual abundances from LAMOST. Other data-driven methods include *The Payne* (Ting et al. 2019), which, like *The Cannon*, works by explicitly modeling spectra as a function of labels (stellar parameters and abundances), and that of Leung & Bovy (2019), which uses a convolutional neural network to estimate labels directly from spectra without explicit inference. Xiang et al. (2019) recently released a catalog of 16 abundances (C, N, O, Na, Mg, Al, Si, Ca, Ti, Cr, Mn, Fe, Co, Ni, Cu, and Ba) for LAMOST DR5

using a neural-net-based model calibrated by both labeled spectra (using overlap between LAMOST and both APOGEE and GALAH) and physical modeling. This work has many common aspects with our own but is different in detail. Both calibrate flexible spectral models (a shallow neural network, in the case of Xiang et al. 2019) with labels from high-resolution surveys, but Xiang et al. (2019) also employ gradients of ab initio models. An advantage of using model gradients is that physical expectations are incorporated into the label derivation. Our approach, however, prioritizes the data alone in specifying the model, which can be advantageous when physical models are lacking. Differences between the catalogs for those elements trained using the GALAH labels will help reveal the biases of each approach.

Our approach requires reference objects, stars with high-quality spectra and precise labels (stellar parameters and abundances), that are representative of the survey objects. They are used to calibrate a model that produces synthetic spectra from stellar labels. This model is then used to estimate labels for the full set of survey stars, in our case, the LAMOST catalog. Both the APOGEE and GALAH surveys have stars in common with LAMOST that can serve as possible reference objects. APOGEE provides higher-precision abundance measurements than GALAH, which enables, for example, the clear disambiguation of the low- and high- α sequences, as seen in the radial maps of Hayden et al. (2015) and Nidever et al. (2014). However, the dimensionality of the abundance space measured by APOGEE is low (Ness et al. 2018, 2019; Price-Jones & Bovy 2018) (although note that weak lines of neutron capture elements have been identified in this region; Hasselquist et al. 2016; Cunha et al. 2017). GALAH, on the other hand, provides abundance measurements across a more extensive set of nucleosynthetic channels, including the neutron capture (r and s) processes. The neutron capture element enhancements have been previously explored only through boutique analyses of small samples of stars observed at high resolution (e.g., Bensby et al. 2014; Spina et al. 2018) and in the solar neighborhood, to which GALAH is largely confined (e.g., Buder et al. 2019; Schönrich & Weinberg 2019). GALAH also provides abundances for main-sequence stars, allowing us to extend our modeling to that regime.

We want to explore the promise of the largest number of element abundance families as possible, so we took the roughly 10,000 stars in common between GALAH and LAMOST to build a model using the LAMOST spectra and GALAH stellar parameters and abundances. While the GALAH labels are less precise than those from APOGEE and thus yield less precise LAMOST labels, the LAMOST catalog is large enough to enable very precise mean estimates of abundances on a population basis (e.g., Blancato et al. 2019; Ness et al. 2019). Using GALAH as a source for our input labels allows us to propagate r -process and s -process abundances to the outer disk and halo.

In deriving a set of individual abundances for LAMOST, this work complements the LAMOST catalog, which provides stellar parameters and bulk metallicity (a term used interchangeably with $[\text{Fe}/\text{H}]$ in this work) only. We deliver inferred abundances for elements from five nucleosynthetic families: *light* elements, which are dispersed by asymptotic giant branch (AGB) stars and core-collapse supernovae (CCSNe), and whose atmospheric abundances can change owing to dredge-up; α -elements, which are dispersed primarily by CCSNe; *iron-peak* elements, which are dispersed by both CCSNe and SNe Ia; *odd-Z* elements, which are dispersed by both CCSNe

and SNe Ia and expected to display similar trends to the α -elements; s -process elements, which are thought to be produced and dispersed in AGB stars; and r -process elements, which are produced in extremely neutron-rich environments. It is not clear at present whether neutron star mergers are the primary site of the r -process, or if other sites make appreciable contributions (e.g., Arnould et al. 2007; Côté et al. 2018; Hansen et al. 2018; Sakari et al. 2018, 2019; Siegel et al. 2019). For each star, we deliver five (for dwarfs) or six (for giants) abundances of O (light), Eu (r -process), mean α , Sc (iron-peak), mean s -process, Mg (α), Al (odd Z), Mn (iron-peak), and Ba (s -process). Having derived these abundances, we demonstrate the scientific value of multielement abundances of large numbers of stars. We do this using pairs of stars across the disk and halo, examining the abundance similarity of wide binaries, that have been identified by their kinematics alone. We also map the chemodynamical abundance structure of the disk and halo, making links to signatures of evolution such as radial migration and Galaxy assembly.

In Section 2 we describe the GALAH and LAMOST data and the quality cuts we applied. Section 3 provides a brief overview of *The Cannon*. In Section 4 we discuss model checks and evaluate the error of our label estimates. Section 5 discusses our public catalog and key scientific results, and Section 6 discusses their implications.

2. Data

Our data comprise the $R = 1800$ DR4 v2 LAMOST spectra, the $R = 28,000$ DR2.1 GALAH spectra, and stellar parameter and abundance labels (Buder et al. 2018), as well as the Gaia proper-motion and parallax measurements for our stars. From GALAH we use T_{eff} , $\log(g)$, v_{mic} , and $[\text{Fe}/\text{H}]$, along with abundances with respect to Fe, of O, Si, Ca, Ti, Eu, Sc, Y, Mg, Al, Mn, and Ba. Figure 1 shows the Galactic footprints of GALAH and LAMOST. A portion of each survey's spectrum for a typical training set star is shown in Figure 2.

2.1. Quality Cuts and Data Cleaning

One of the formal assumptions of *The Cannon* is that the training labels are known exactly, so constructing a high-fidelity training set is crucial. To build our training set, we first determined the set of stars in common between GALAH and LAMOST. We performed a $1''$ sky match between GALAH DR2.1 and LAMOST DR4 v2 to identify these reference object candidates, of which there were roughly 10,000. We then removed all stars from the potential training set with signal-to-noise ratio (S/N) less than 30 in either the LAMOST z band (snr_z) or the GALAH blue channel (snr_{c1}). We also removed any star for which $\text{chi2}_{\text{cannon}}$ (a column in the GALAH catalog, not a product of our analysis) was greater than 4, which indicates that the best-fit spectral model is a poor fit to the whole spectrum, and any star for which $\text{flag}_{\text{cannon}}$ was nonzero, which can indicate a variety of problems with abundance determination. These cuts removed roughly half of the stars from consideration.

We found that cutting on the reported GALAH label errors did not improve our performance against the validation set. To further exclude low-quality measurements from our training set, we therefore generated and evaluated the fit of the best-fit *Cannon* model spectrum for each reference stellar spectrum, for every element in the GALAH catalog. The GALAH pipeline uses separate *Cannon* models for each elemental abundance in

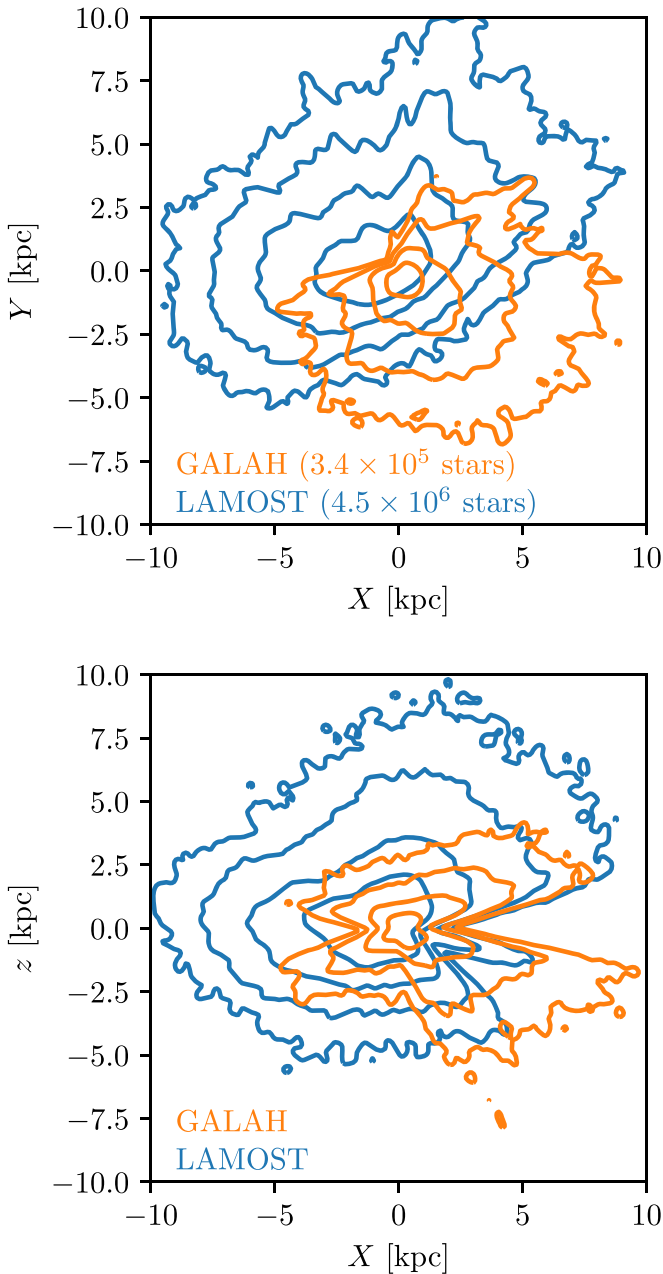


Figure 1. Face-on (top) and edge-on (bottom) contours in surface density ($5 \times 10^{4,3,2,1} \text{ kpc}^{-2}$) shown in heliocentric Galactic coordinates for GALAH and LAMOST, which probes much farther into the outer disk and halo. The Galactic center is at $X = 8 \text{ kpc}$, $Y = 0$.

order to restrict each model to the wavelengths of unblended lines. Each model has different best-fit parameters, which we were not able to retrieve. They are, however, within the errors of the mean reported stellar parameters for each star (Buder et al. 2018). For the stellar parameter labels, we used the values in the GALAH DR2.1 catalog,¹² along with A_K values calculated with the Rayleigh–Jeans color excess method (Majewski et al. 2011) applied to ALLWISE (Wright et al. 2010; Mainzer et al. 2011) and Two Micron All Sky Survey (2MASS; Skrutskie et al. 2006) broadband photometry, as was done for the GALAH models. We calculated χ^2 between the best-fit GALAH model and the observed GALAH spectrum for

every star in our training set in the region of the strongest lines of each element (the `chi2_cannon` flag pertains to the global fit). Appendix C lists the wavelength regions used, which are the same windows used in the GALAH pipeline. The distribution of χ^2 values for some elements peaked lower than expected from nominal measurement error alone by a factor of 2–3, meaning that a cut on some multiple of χ^2/dof was not theoretically justified. We removed all stars with χ^2 values above the 85th percentile, for any of its abundances. This led to a significant improvement in our cross-validation (CV) results, as discussed in our methods, on the order of 15%–40%. Using the 75th percentile, as a more conservative cut, gave us no improvement in CV tests. These cuts leave 1722 stars in the training set. We do not exclude stars flagged in GALAH based on `flag_x_fe` because we performed our own per-abundance χ^2 cut and because removing stars where the GALAH model may be extrapolating reduces the size of our training set too drastically. We emphasize, however, that *The Cannon* is likely to extrapolate well for many abundances.

2.2. Dwarf and Giant Models

After the quality cuts described in Section 2.1, we were left with a training set that spans the Kiel diagram and metallicity (Figures 3, 4). We modeled giants and dwarfs separately, with the division between models given in terms of LAMOST $\log g$ and T_{eff} by

$$\log g = \begin{cases} 4.18 & T_{\text{eff}} < 5200 \text{ K} \\ (-6 \times 10^{-4})T_{\text{eff}}/\text{K} + 7.3 & T_{\text{eff}} \geq 5200 \text{ K}. \end{cases} \quad (1)$$

The split gives us 532 giants and 1190 dwarfs as our reference objects. The values in Equation (1) to separate dwarfs and giants are somewhat arbitrary. We find that each model performance is not sensitive to these precise values. We decided which elements to infer for each model by balancing our ability to recover each abundance in CV (Section 4) with the objective of having several elements across a nucleosynthetic channel. For both models, we include T_{eff} , $\log g$, v_{mic} , $[\text{Fe}/\text{H}]$, $[\text{O}/\text{Fe}]$, and $[\text{Eu}/\text{Fe}]$ as labels. For the dwarfs, we also used iron-relative abundances of error-weighted mean α (from Mg, Si, Ca, and Ti), Sc, and error-weighted mean s -process (from Ba and Y), while for the giants we also used Mg (α), Al (odd- Z), Mn (iron-peak), and Ba (s -process). Training a model without α or Mg yields a systematic offset in inferred neutron capture abundances, likely because the model will exploit correlations between these nucleosynthetic families if they are not controlled for.

We only used mean abundances in the same nucleosynthetic family if they appeared strongly correlated in the training set. We tried using dereddened Gaia G -band magnitude instead of $\log g$, which would allow us to apply a prior at test time, but we found that this did not improve our results in practice. The model had trouble predicting extinction, partially because our training sets do not include any high-extinction stars. Including extinction as a label did not improve our ability to predict any of the abundances, so we opted not to.

For subsequent analysis, we cross-matched with Gaia by taking the source within $1''$ of the LAMOST star with the lowest G -band magnitude. Throughout this paper, we use of the parallactic distance estimates from Bailer-Jones et al. (2018), which makes use of a prior incorporating the expected galactic spatial distribution. Other distance catalogs (e.g., Anders et al. 2019) will have different biases for stars with uncertain

¹² Available at <https://docs.datacentral.org.au/galah/>.

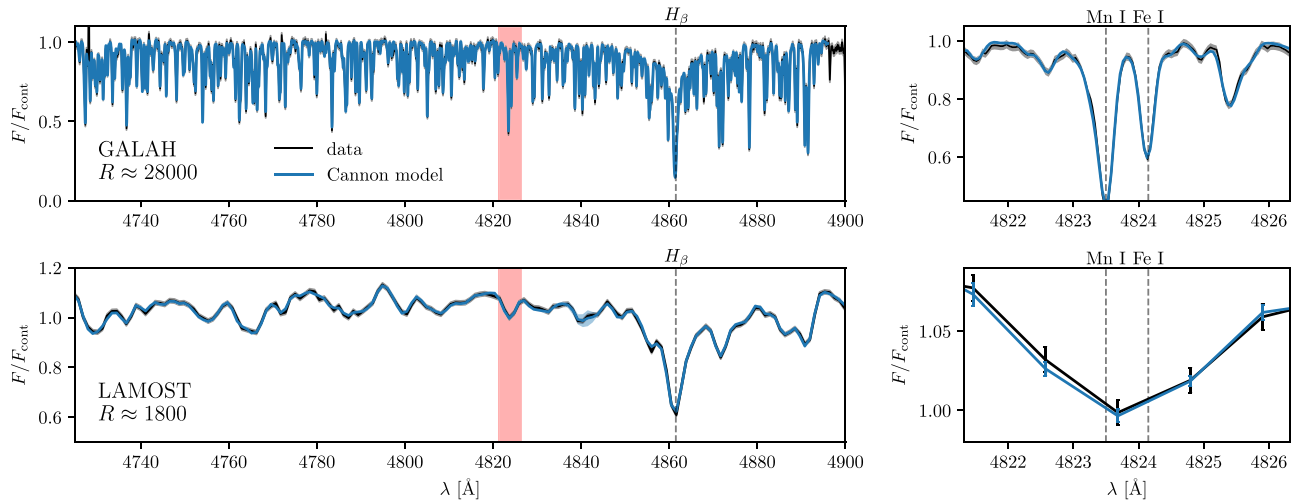


Figure 2. Comparison of the GALAH and LAMOST spectra for the same star, 2MASS 00010184+0407201, Gaia DR2 2740354684364096000. The top panels show part of the star’s GALAH spectrum ($S/N = 65$) and the *Cannon* model, while the bottom two show the same for LAMOST ($S/N = 179$). On the left, note the large $H\beta$ line and surrounding features, on the right, observe the fit around a known Mn feature (highlighted in red on the left). Both the measured spectra and *Cannon* models are shown with their 1σ errors, shown with error bars in the right panels and a shaded region in the left panels.

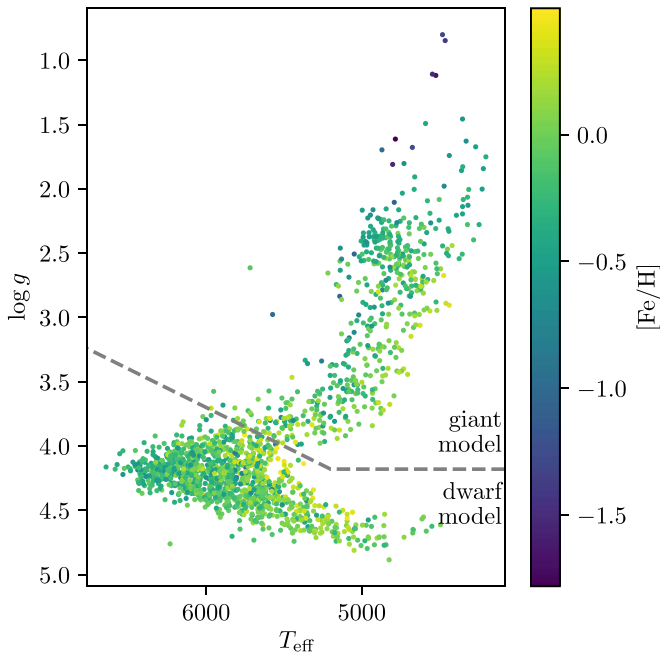


Figure 3. Our 1722 training stars in the LAMOST Kiel diagram space colored by (GALAH) $[Fe/H]$. Since there are more metal-poor stars in the giant training set, our giant model is unbiased down to lower metallicity.

distances (e.g., those far from the Sun), so quantitative results derived from our catalog will be conditioned upon the assumptions of Bailer-Jones et al. (2018). Our results below are largely qualitative and unlikely to be strongly dependent on choice of distance catalog. Figure 5 shows the mean fractional distance error as a function of Galactocentric radius, R . Distance errors blur our maps of chemistry across the Galaxy (Section 5.3), particularly far from the solar annulus, where they reach 20%.

3. Model

The following is a brief description of *The Cannon* (see Ness et al. 2015, for a more extended discussion). For this work we

build a JULIA-based implementation of *The Cannon*, which is documented and available at this URL¹³ and via the JULIA package manager. The source code uses the same nomenclature as the description here and allows for optional masking of labels (self-consistent training with the model constrained so that each label is only “on” at specified wavelengths).

For each star, n , we take the flux value in the spectral pixel with wavelength λ to be $F_{n\lambda}$ and its (Gaussian, independent) measurement uncertainty to be $\sigma_{n\lambda}$. To prepare the spectra for *The Cannon*, we first redshift-corrected the spectra using the z value provided in the LAMOST data table and interpolated each star to a common wavelength grid. We then continuum-normalized the spectra by dividing out the continuum, approximated by smoothing the spectra with a Gaussian kernel with a 50 \AA standard deviation, truncated at 150 \AA from the center, in the same manner as Ho et al. (2017a, 2017b). This normalized flux is then near unity in the absence of emission or absorption features. For each reference star, we also define ℓ_n to be the vector containing its physical parameters and abundances (its *labels*). These are the quantities we ultimately wish to infer for the rest of the LAMOST spectra, at test time.

Our label vector ℓ_n for each reference star is

$$\ell_n = [T_{\text{eff}} \log(g) v_{\text{mic}} [Fe/H] [X_1/Fe] \dots [X_N/Fe]]^T, \quad (2)$$

where X_1, \dots, X_N are the elements whose abundances we wish to determine. It is good practice for both numerical stability and model flexibility to express all labels in units such that they are distributed around zero and have similar magnitudes. We do this by subtracting from each label its (training set) mean and dividing it by its (training set) dispersion. This transformation is then undone after the inference has taken place.

In numerous published uses of *The Cannon* (including this one), the flux in each pixel is described by a second-degree polynomial of the elements of the label vector whose coefficients, θ , are determined by a training set of spectra for which, ideally, both accurate and precise labels are available. For a given spectral pixel and star, we then have our spectral flux, F , for our n reference objects at each wavelength, λ ,

¹³ github.com/ajwheeler/TheCannon.jl

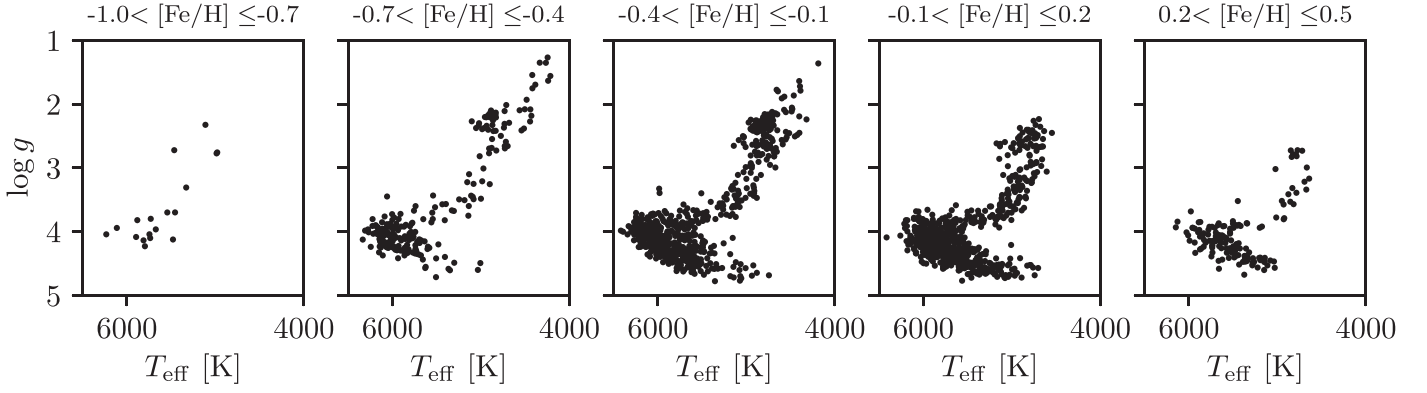


Figure 4. Our 1722 training stars across the (LAMOST) Kiel diagram in bins of metallicity. For the extreme ends of our metallicity range, the lack of training set coverage may bias our estimated labels.

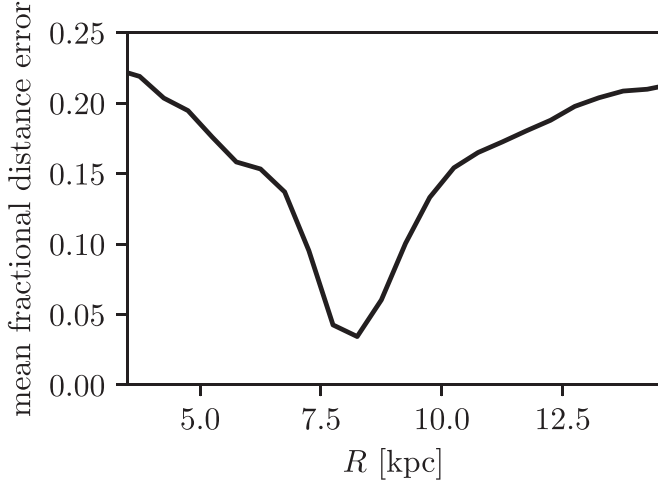


Figure 5. Mean fractional distance error as a function of Galactocentric radius. Distance errors blur chemical maps of the Milky Way far from the solar annulus.

defined as

$$\begin{aligned}
 F_{n\lambda} = & \theta_{\lambda}^0 (\text{constant term}) \\
 & + \theta_{\lambda}^{T_{\text{eff}}} T_{\text{eff}} + \dots + \theta_{\lambda}^{X_N} [X_N/\text{Fe}] (\text{linear terms}) \\
 & + \theta_{\lambda}^{T_{\text{eff}}^2} T_{\text{eff}}^2 + \dots + \theta_{\lambda}^{X_N^2} ([X_N/\text{Fe}]^2) (\text{squared terms}) \\
 & + \theta_{\lambda}^{T_{\text{eff}} \log(g)} T_{\text{eff}} \log(g) + \dots \\
 & + \theta_{\lambda}^{X_N X_{N-1}} [X_N/\text{Fe}] [X_{N-1}/\text{Fe}] (\text{cross-terms}) \\
 & + \text{error}.
 \end{aligned}$$

To specify an error model, we can write the above as a likelihood function

$$F_{n\lambda} | \ell_n, \theta_{\lambda}, s_{\lambda} \sim \mathcal{N}(\boldsymbol{\eta}(\ell_n) \cdot \boldsymbol{\theta}_{\lambda}, \sigma_{n\lambda}^2 + s_{\lambda}^2), \quad (3)$$

where \mathcal{N} is the normal distribution, s_{λ} is model uncertainty (either inherent stochasticity or physics that has not been captured by the model) at wavelength λ , $\boldsymbol{\theta}_{\lambda}$ is the vector of coefficients describing how the flux at λ varies with label value, and $\boldsymbol{\eta}$, the quadratic expansion (called the vectorizing function in Casey et al. 2016), maps from labels to every zeroth-, first-, and second-order combination of components of the label vector,

$$\boldsymbol{\eta}(\ell_n) = [1 \ T_{\text{eff}} \ \dots \ [X_N/\text{Fe}] \ T_{\text{eff}}^2 \ T_{\text{eff}} \log(g) \ \dots]^T. \quad (4)$$

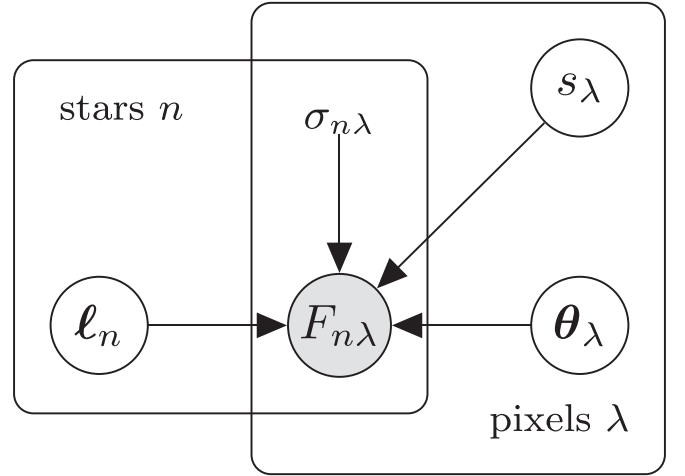


Figure 6. The Cannon likelihood as a probabilistic graphical model. During training, the latent variables in the “stars” panel (ℓ_n) are fixed using stars for which labels are known, in our case from GALAH. When inferring stellar labels, the latent variables in the “pixels” panel (θ_{λ} and s_{λ}) are fixed to their point estimates from training and the maximum likelihood estimates for all ℓ_n are calculated.

If ℓ_n is a vector of length N , $\boldsymbol{\eta}(\ell_n)$ is a vector of length $(N^2 + 3N)/2$. A more flexible model could be constructed by replacing $\boldsymbol{\eta}$ to an expansion with higher-order terms, or to other combinations of labels. However, quadratic models have been shown to be sufficient in practice (Ness et al. 2015, 2016, 2019; Ho et al. 2017a, 2017b). In fact, a linear model is often all that is needed (Birky et al. 2020; Hogg et al. 2018). The combinatoric increase in model parameters that would be necessary for a higher-order polynomial is undesirable.

Figure 6 shows the likelihood function as a probabilistic graphical model, which depicts the relationships between observed and latent quantities. Ideally, the full joint distribution over training data and output labels would be sampled from directly (with e.g., Markov Chain Monte Carlo), but such an approach is not computationally feasible. Instead, the problem is divided into a training step, in which a point estimate of each θ_{λ} and s_{λ} is estimated from the training set, and an inference step, in which the labels of each star are estimated.

During the training step, each θ_{λ} and s_{λ} is jointly fixed to its maximum likelihood estimate (MLE), given the labeled spectra in the training set. For fixed s_{λ} , the model is linear with fixed

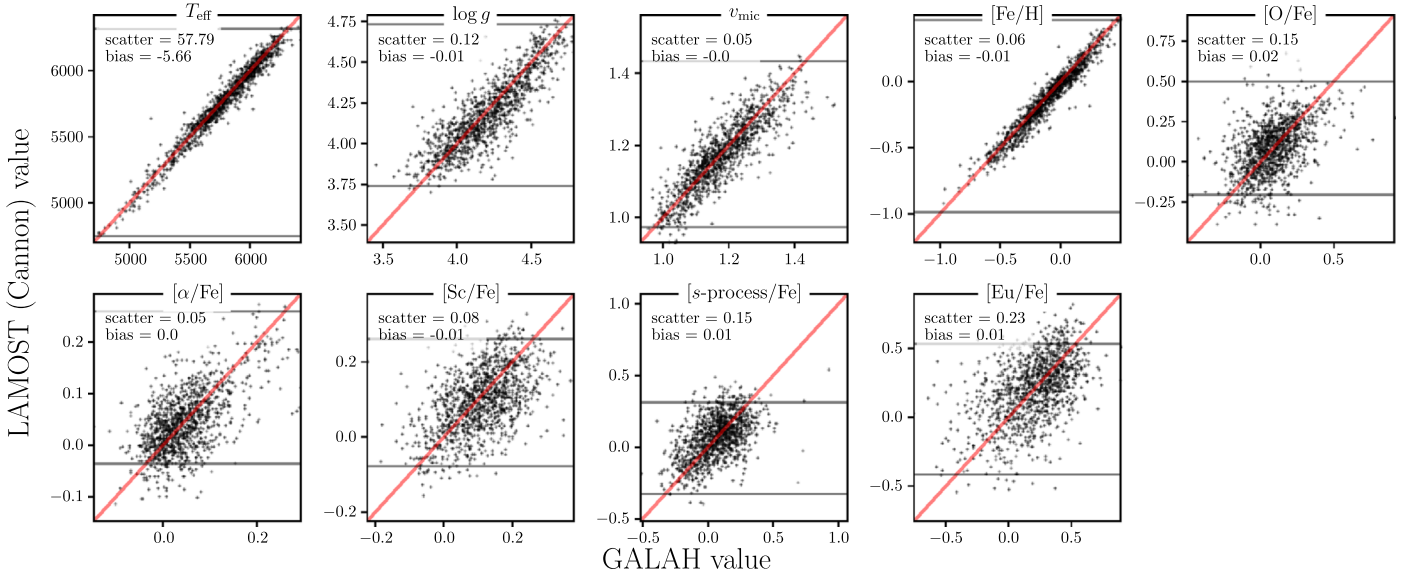


Figure 7. CV recovery of training set labels for the dwarf model. Horizontal lines show boundaries beyond which the model is biased or unprobed by the training set.

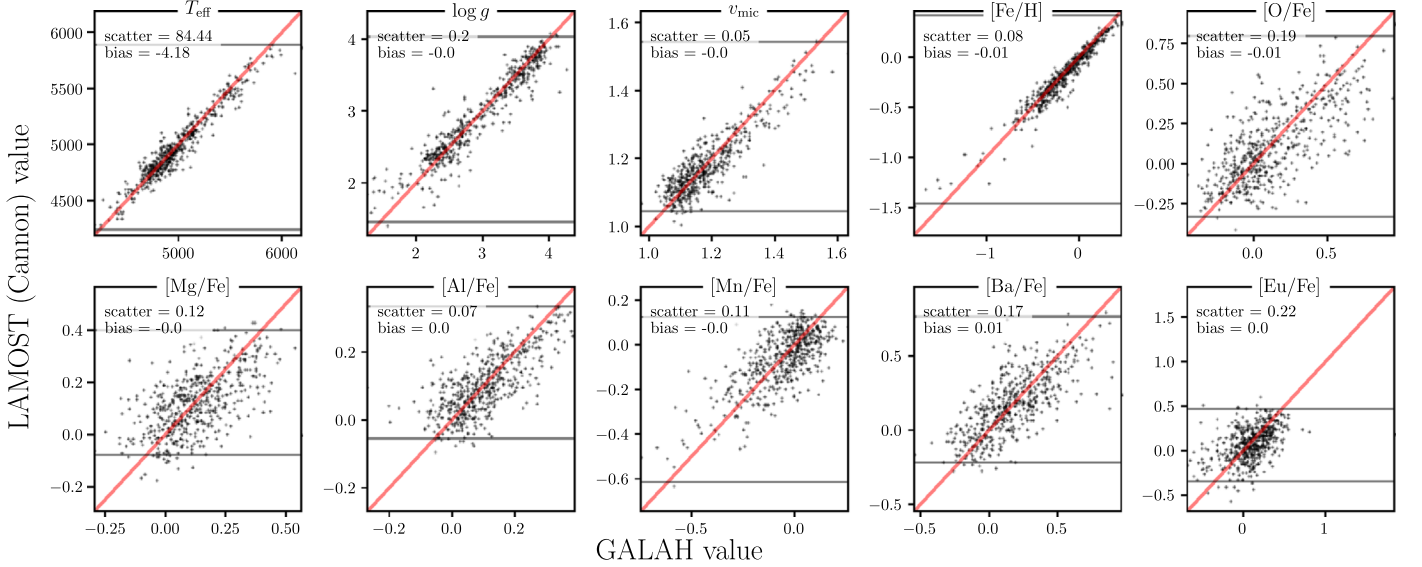


Figure 8. Analogous to Figure 7; CV recovery of training set labels for the giant model. Horizontal lines show boundaries beyond which the model fails to extrapolate. While the scatter in [Fe/H] is higher at lower values, the model appears to be nearly unbiased down to [Fe/H] ≈ -1.5 .

Gaussian error in θ_λ , so its MLE, $\hat{\theta}_{|s_\lambda}$, can be calculated analytically. Finding \hat{s}_λ is then a matter of numerically maximizing the log-likelihood,

$$\log \mathcal{L}(s_\lambda) = -\sum_n \frac{1}{2} \left(\frac{(\eta(\ell_n) \cdot \hat{\theta}_{|s_\lambda} - F_{n\lambda})^2}{\sigma_{n\lambda}^2 + s_\lambda^2} + \ln(\sigma_{n\lambda}^2 + s_\lambda^2) \right) + \text{const}, \quad (5)$$

in one dimension. During the inference step, the MLE of ℓ_n is calculated with s_λ and θ_λ fixed to their point estimates. There is no trick to get us out of multivariate optimization here, since η is nonlinear.

4. Model Evaluation

We use 12-fold CV in order to verify that the model is able to recover stellar labels. We partition the reference objects into

12 random subsets and then predict the labels of each subset using the other 11 as training data. This gives us a prediction for each reference star that has not leveraged its GALAH labels. Figures 7 and 8 show CV performance for the giants and dwarfs, respectively, along with the scatter, bias, and correlation coefficient for each label. Our CV-assessed abundance precision ranges from 0.05 to 0.23 dex for dwarfs and from 0.07 to 0.22 dex for giants. Examination of the labels inferred for spectra from repeat observation of the same star shows differences consistent with CV precision.

We also use CV to identify the thresholds beyond which our model is highly biased or unprobed by the training data. We say that the model is in this regime when it under- or overpredicts the label being considered 90% of the time in CV. The specific calculation is as follows: For a given label, l (e.g., $l = T_{\text{eff}}$), we approximate $p(l_{\text{true}}, l_{\text{inferred}})$ with a kernel-density estimate with bandwidth chosen by Silverman’s rule (Silverman 1986) and

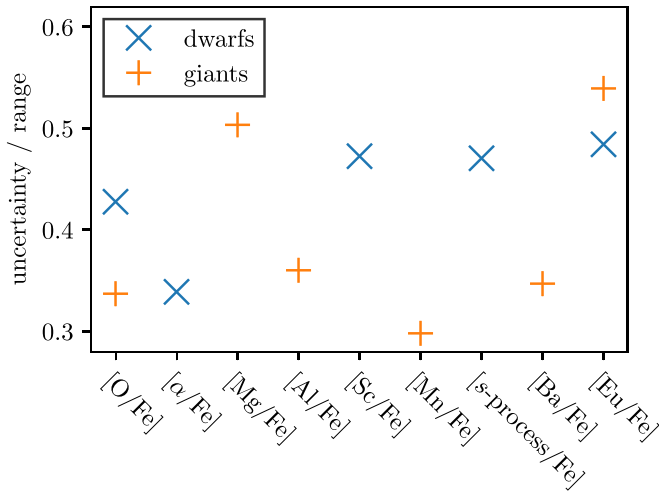


Figure 9. Precision of each of our abundances relative to the range over which the model is approximately unbiased. We generally infer abundance ratios with precision at the 30%–50% level. Smaller values indicate higher relative precision of that abundance and presumably higher discriminating power between stars.

then use this approximate distribution to find the values of l_{inferred} at which $p(l_{\text{true}}|l_{\text{inferred}})$ excludes l_{inferred} at the 90% level. These boundaries are shown as horizontal lines in Figures 7 and 8. Stars that fall beyond these boundaries are flagged in our catalog. Figure 9 shows the precision (twice the scatter in Figures 7 and 8) of each of our abundances relative to the range over which the model is roughly unbiased. This quantity is often what is relevant when comparing the labels of different stars, rather than characterizing a single star.

4.1. Model Interpretability

The Cannon is simple enough that its parameters are open to direct interpretation. This sets it apart from more complex modeling approaches such as neural networks.

It is clear, for example, that our model learns T_{eff} in large part from the Balmer series, as this is where $\theta_{T_{\text{eff}}}$ becomes large. By examining model scatter, s_{λ} , as a function of wavelength, we can tell that our model is less precise in the regions of CN bands, at the beginning of the spectral region of LAMOST. In some wavelength regions, s_{λ} drops to 0, likely because continuum normalization introduces small correlations between nearby pixels that are not accounted for by the model. It is also apparent that the model is leveraging the whole spectrum to predict abundances, rather than strong lines only. We performed tests by isolating only regions where individual abundance features are present in the spectra, fixing the model coefficients to zero outside these regions at training time. This approach is similar to the way in which GALAH determined their abundance labels, using abundance windows. For the LAMOST spectra, this approach of using windows fails to recover abundance ratios in CV. Section 5.1 discusses some implications of this fact, and our scatter and linear coefficients are plotted as a function of wavelength in Appendix A.

5. Results

5.1. Catalog

We produce a catalog of stellar parameters and individual abundances for 4,541,883 observations of 3,744,284 stars

across the Kiel diagram (Figure 10), which is available online,¹⁴ along with our model coefficients and training set. We combine observations of the same star by reporting (z -band) S/N-weighted averages of their labels. Along with our inferred stellar parameters and abundances, we provide the LAMOST and Gaia identifiers for each star, as well as its Galactic position, radial velocity (RV), and estimated actions. We also provide windowed and whole-spectrum χ^2 values and flags to tell when the model is extrapolating. For each star, we calculated approximate actions with *galpy* (Bovy 2015) using the Stäckel fudge (Binney 2012; Bovy & Rix 2013) and *MWPotential2014*, applied using Gaia distances (Bailer-Jones et al. 2018) and proper motions, and LAMOST RVs. While Gaia achieves a better RV precision (see Figure B1), Gaia RVs are only available for approximately one-fifth of our catalog. We assumed that the Sun sits at $X = 8$ kpc, $z = 0.025$ kpc (Jurić et al. 2008) and is moving with $v_X = 11.1$ km s⁻¹, $v_Y = -232.24$ km s⁻¹, $v_Z = 7.25$ km s⁻¹ (Schoenrich & Binney 2009). Table 1 provides the full catalog schema. To understand the effect of RV and distance uncertainty on our estimated actions, we sampled their values from their error distribution and calculated Galactocentric coordinates and actions for each iteration, performed 20 times. The median uncertainties for J_R , J_ϕ , and J_z , respectively, were 5, 21, and 1 kpc km s⁻¹. Appendix D explores these errors in more detail.

Here we highlight several caveats to the use of these data:

1. We allow our model to take leverage of the full information content of the spectrum. It therefore learns not only from the most fundamental features of each label but also from correlated features (as we can identify using our model coefficients, which is an advantage of a simple interpretable model). Examination of the model’s coefficients reveals that the whole spectrum is leveraged in order to predict each abundance. Our CV tests show that our model works. It performs well with no hyperparameter tuning, and our analysis of wide binaries in the solar neighborhood (El-Badry et al. 2019) is indicative of the additional discriminating power beyond an overall metallicity these abundances provide (see Section 5.2). However, the abundances are not being measured directly. The fidelity of our predicted labels relies on our reference objects (confined to the solar neighborhood) being representative of the survey data. For this reason, our reported abundances may be more accurate for disk stars than halo stars. In order to identify many cases where the model fails to generalize from the training set, we provide χ^2 values calculated across the whole spectrum and individually in narrow windows centered on strong lines, for each element. If the best-fit spectrum is a poor fit around known features of a given element, it is likely highly enriched or depleted in that element. In fact, this approach is a good way to find such stars with anomalous abundance patterns. Indeed, Casey et al. (2019), Kemp et al. (2018), and Norfolk et al. (2019) have used the departure of a basic stellar parameter model generated with *The Cannon*, from the spectra, to find LAMOST stars that are enhanced in Li, K, and Ba and Sr, respectively.

¹⁴ <https://doi.org/10.7910/DVN/5VWKMK>

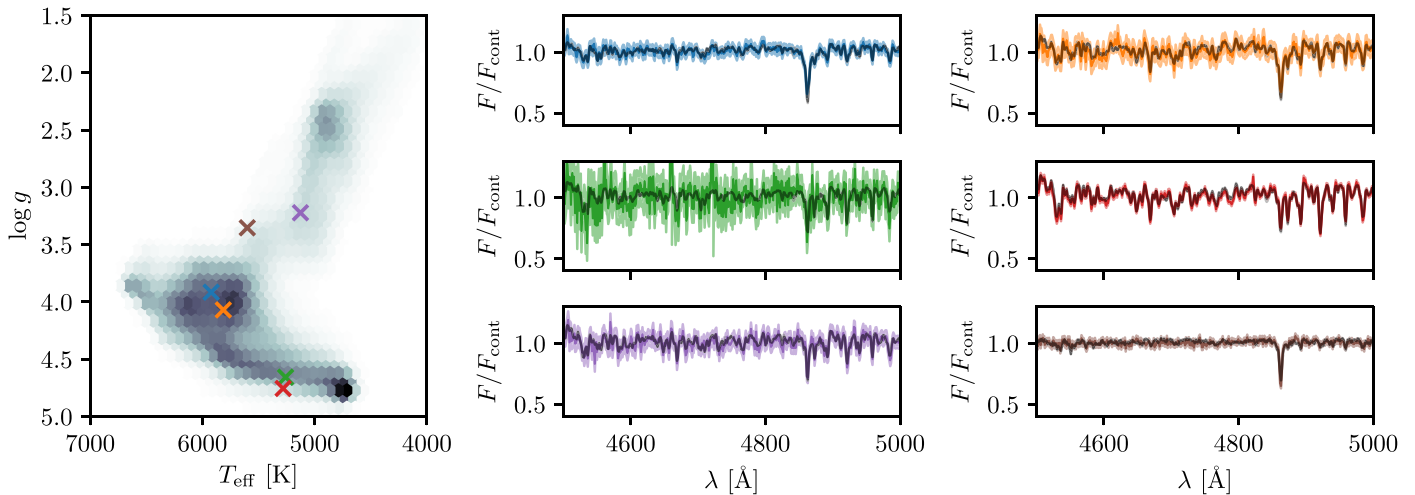


Figure 10. Portion of the best-fit model spectra (black) and real data (colored), both with 1σ uncertainties, for six randomly chosen stars in our catalog. Though simple, the model is flexible enough to fit the data across the Kiel diagram.

2. A caveat that is general to data-driven methods is that the model will not necessarily extrapolate correctly outside the parameter space spanned by the training set (see Figure 4). We provide flags to indicate when individual abundances are in the regime where they may be incorrectly extrapolated, as well as a flag indicating when T_{eff} , $\log(g)$, v_{mic} , or $[\text{Fe}/\text{H}]$ may be incorrectly extrapolated (Table 1). We determine when our model is extrapolating as described previously, in Section 4.
3. While error estimates for each abundance ratio are desirable, producing accurate ones would be prohibitively costly with our current inference infrastructure. We advise the user to utilize our CV-assessed error and caution them to be aware that treating our abundance estimates as homoscedastic is a necessary compromise.
4. Examination of open clusters in our catalog reveals that our inferred abundance ratios for dwarf stars are subject to strong systematics as a function of T_{eff} . There are astrophysical explanations for weak abundance trends with T_{eff} and $\log(g)$, such as atomic diffusion (Dotter et al. 2017; Gao et al. 2018; Souto et al. 2019), but not trends of this magnitude. Similar systematics are present in the GALAH DR2 internal catalog (which employs the same analysis pipeline as the public release), as well as the official LAMOST $[\text{Fe}/\text{H}]$ values for dwarfs, suggesting that these trends are not introduced by our label transfer but are present in ab initio stellar models and possibly inherited via our training set. There are no obvious systematics in the red giant stars in our catalog, save for $[\text{Ba}/\text{Fe}]$, discussed below. However, LAMOST does not contain enough red giants in known open clusters or wide binaries to determine the presence and magnitude of any systematics conclusively.

Figure 11 shows systematic trends in Praesepe in $[\text{Fe}/\text{H}]$ as a function of T_{eff} by plotting our inferred values (for stars selected by Gaia Collaboration et al. 2018) alongside GALAH internal DR2 values for the same open cluster, which is expected to be chemically homogeneous to a level well below our precision. GALAH internal DR2 includes stars not part of the public DR2, but it employs the same analysis pipeline. Trends of the type exhibited in Figure 11 are reduced but not eliminated in

GALAH DR3 (A. Buder et al. 2020, in preparation). Other abundances exhibit similar behavior. This indicates that systematic error as a function of stellar parameters is a major contributor to our abundance error (see also Section 5.2). To the extent that these trends are physical, the recommendation that the catalog user compare stellar abundances within a narrow range of T_{eff} remains.

The systematic trends we see in dwarf abundances could be “calibrated out” using the nearly 3000 stars in LAMOST DR4 open clusters (with two or more targets; Cantat-Gaudin et al. 2018) and 142 known wide binaries (El-Badry et al. 2019). Instead of applying a post hoc correction, they could also be used to constrain the model at training time. Correcting for these systematics in the dwarf population is beyond the scope of our analysis. Despite this systematic effect, our abundances for dwarf stars are still useful for conducting analyses in restricted temperature ranges (see, e.g., our examination of abundances of wide binaries in Section 5.2). When examining the abundance trends across the disk, we exclude the dwarf stars and focus on the $\approx 1 \times 10^6$ red giant stars in our catalog. These giants span a vast spatial extent and alone demonstrate the scientific potential of the distribution of stellar abundance data across the Galaxy.

Unless otherwise stated, in the sections below we employ stars in our catalog for which $\text{chi}2$ is less than 7000. Other cuts were not found to have an effect on the results presented below.

5.2. Detailed Abundances of Wide Binaries

El-Badry et al. (2019, hereafter EB19) used Gaia to identify wide binaries in the solar neighborhood and examined their properties as a function of $[\text{Fe}/\text{H}]$. We examined the detailed abundances of those present in LAMOST. For ease of analysis, we excluded pairs for which T_{eff} or $\log(g)$ was not available and those containing at least one giant (a total of eight pairs). Because of the strong systematic trends with T_{eff} that are present in our dwarf abundances, we constrain our analysis to wide binaries with $\Delta T_{\text{eff}} < 250$ K, for which both stars are LAMOST dwarfs.

Table 1
Catalog Schema

Column Name	Type	Unit	Description
source_id	integer		Gaia DR2 source id
designation	string		LAMOST unique star identifier
giantmodel	boolean		True if labels were estimated with giant model
teff	float	K	T_{eff}
logg	float		$\log(g)$
vmic	float		v_{mic}
kiel_extrap	boolean		True if T_{eff} or $\log(g)$ (the axes of the Keil diagram) are in regime where model fails to extrapolate for any observation
chi2	float		Whole-spectrum χ^2
fe_h	float		[Fe/H]
fe_h_extrap	boolean		True if [Fe/H] value is in regime where model fails to extrapolate for any observation
x_fe	float		[X/Fe]
chi2_x_fe	float		χ^2 calculated in windows around strong lines of X
x_fe_extrap	boolean		True if [X/Fe] value is in regime where model fails to extrapolate for any observation
snr_z	float		LAMOST z-band S/N
ra	float	deg	Right ascension
dec	float	deg	Declination
R	float	kpc	R , in Galactic cylindrical coordinates
phi	float	rad	ϕ , in Galactic cylindrical coordinates
z	float	kpc	z , in Galactic cylindrical coordinates
vR	float	km s ⁻¹	R -velocity
vT	float	km s ⁻¹	ϕ -velocity
vz	float	km s ⁻¹	z -velocity
JR	float	kpc km s ⁻¹	Radial action
Jphi	float	kpc km s ⁻¹	Angular momentum
Jz	float	kpc km s ⁻¹	Vertical action

Note. Here, x and X stand for each of the chemical symbols for the elements whose abundances are being estimated. Our Galactic coordinate system is right-handed. We also make available the table of per-observation labels.

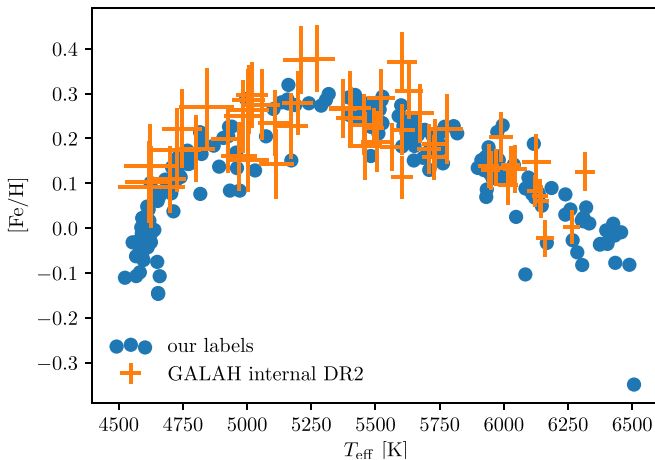


Figure 11. Inferred [Fe/H] vs. effective temperature for LAMOST and GALAH dwarfs in Praesepe. The GALAH values come from internal DR2, which used the same analysis pipeline as the DR2 values in our training set. The systematic trend with T_{eff} is spurious, since all stars in Praesepe have the same abundances to below the precision achievable with low-resolution spectra.

To confirm the additional discriminating power of our inferred abundances, we examined the abundance similarity of wide binaries compared to a reference sample of nonbinary pairs. We constructed a set of random pairs of field stars, where each pair has the same metallicity as the binary pair. The reference stars also conform to the quality cuts made in EB19 with $T_{\text{eff}} < 250$ [K]. We used rejection sampling to ensure that they had as closely as possible the same $\Delta[\text{Fe}/\text{H}]$ distribution

as the EB19 sample. By comparing the abundance distribution of the random field pairs with the wide binaries, we can characterize the amount of information contained in our detailed abundances *above and beyond* that contained by the bulk metallicity, [Fe/H]. To capture the difference in chemistry between stars, we use precision-scaled Euclidean distance,

$$\sqrt{\sum_i \left(\frac{\Delta[X_i/\text{Fe}]}{\sigma_i} \right)^2}, \quad (6)$$

where the X_i 's are the elements estimated and the σ_i 's are their CV-assessed uncertainty. Figure 12 shows the distribution of these chemical distances for both the wide binaries and the field pairs with the same $\Delta[\text{Fe}/\text{H}]$ distribution. The difference between these distributions shows that detailed chemical abundances provide additional information about stars' birth sites. Each abundance included pushes the chemical difference distribution of the binaries and random pairs farther apart. The wide binaries peak at a smaller chemical distance than the reference pairs. Wide binaries peak at a distance of 0.8, and reference stars peak at a distance of 2.5. This is consistent with findings that the majority of wide binaries are chemically identical to at least the 0.1 dex level (Andrews et al. 2018, 2019; Hawkins et al. 2020). We did not find that binaries with a larger separation are more chemically different, in contrast with the results of Ramirez et al. (2019).

If a cut in ΔT_{eff} is not made, the systematic error in each abundance becomes similar in magnitude to the dispersion of chemistry in the solar neighborhood (0.1–0.5 dex, depending on abundance). Without this ΔT_{eff} cut, and with this subsequent

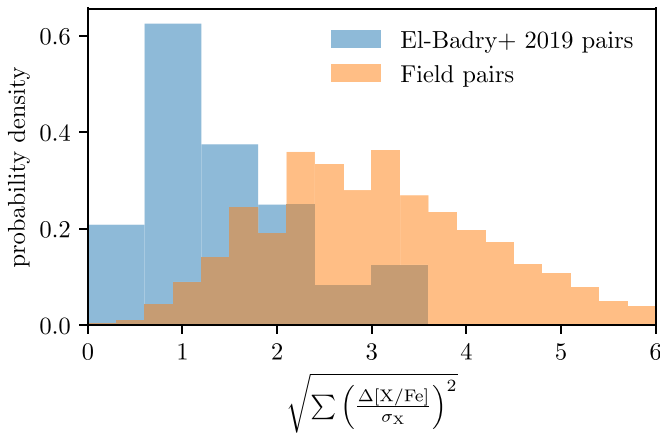


Figure 12. Error-weighted chemical distances for EB19 wide binaries and for random field pairs selected with the same cuts and chosen to have the same $\Delta[\text{Fe}/\text{H}]$ distribution as the EB19 sample. The wide binaries are more chemically similar than implied by their similarity in bulk metallicity alone.

high systematic error, random field pairs and wide binaries appear to have very similar chemical difference distributions. Even more stringent requirements for ΔT_{eff} result in even more distinct chemical distance distributions for the wide binaries, but at the expense of the number of qualifying wide binaries. In fact, the chemical differences we see in the wide binaries are much smaller than the error we get in CV. This suggests that systematic T_{eff} -dependent effects dominate our CV-assessed errors (see Figure 11). If, in future work, we were able to reduce or eliminate this effect, perhaps by conditioning a model on chemically homogeneous open clusters, we could produce much higher fidelity detailed abundances. Currently, scientific exploitation of our ≈ 3 million dwarf stars should employ narrow ranges of T_{eff} .

Our tests of the chemical differences between wide binary stars indicate not only that the detailed chemistry provides evidence of a common birth site. They also show that systematic effects are a large fraction of our error budget—a promising sign that we can do better with low-resolution spectra in the future.

We also similarly investigated the chemical differences for a sample of comoving pairs in Kamdar et al. (2019) compared to a reference set of field stars at the same $[\text{Fe}/\text{H}]$ and found that they were also chemically more similar than an equivalent set of field pairs, although less so than the wide binaries. Simpson et al. (2019) used GALAH abundances to determine whether 15 comoving pairs found in Gaia were conatal; the same approach could be used here.

5.3. Mapping Chemistry in the Milky Way

We have one of the largest homogeneous samples of stellar abundances. This sample is ideal for mapping the abundance distribution of the Milky Way across a large spatial extent. First, we map the disk across the meridional plane, (R, z) , to characterize the spatial abundance trends in that plane. Similar maps can be created with a different set of abundances using APOGEE, but that data set is most concentrated to the disk and the inner Galaxy, while the LAMOST giants more extensively span the halo and outer disk. APOGEE data clearly reveal the flaring in intermediate-age populations in the (R, z) plane (e.g., Ness et al. 2016). This is presumably a consequence of radial migration (e.g., Roškar et al. 2008), whereby stars increase in

scale height as they move outward in the disk (Minchev et al. 2012). Due to the correlations between abundances and ages (Bedell et al. 2018; Feuillet et al. 2018, 2019; Ness et al. 2019), we might expect to also see such flaring in mean abundance maps, although this is potentially confounded by the metallicity dependence of the age–abundance relationships (Ness et al. 2019). Detailed analyses of the chemodynamical distribution across (R, z) that seek to make any quantitative claims require a careful consideration of the LAMOST selection function. Characterization of the flaring profile of the disk also requires stellar ages, as noted by Minchev et al. (2014, 2018). Here, we aim to show the potential of these data for more in-depth analysis that accounts for the selection function.

Figure 13 shows the (R, z) plane colored by mean label value for nearly 800,000 giant stars, for abundance ratios of Fe, O, Eu, Mg, Al, Mn, and Ba, as well as T_{eff} and $\log(g)$. These maps span $-4 \text{ kpc} < z < 4 \text{ kpc}$ and $7.5 \text{ kpc} < R < 15 \text{ kpc}$. The disk is clearly distinct from the halo. At $R = 8 \text{ kpc}$, for example, the halo transition appears as a smooth mean abundance change centered on $|z| \approx 2 \text{ kpc}$. Flaring is seen in the individual elements, particularly for O, Mg, Eu, and Ba. All of these elements show different flaring, of varying strength and profile. All abundances increase or decrease monotonically with $|z|$ at fixed R , except for $[\text{Al}/\text{Fe}]$, which increases with $|z|$ until $|z| \approx 2 \text{ kpc}$, beyond which it decreases with $|z|$.

The apparent barium-depleted “cone” centered on the Sun is caused by systematic trends in $[\text{Ba}/\text{Fe}]$ as a function of T_{eff} and $\log(g)$, in combination with LAMOST’s selection function. If we plot only the red clump stars as identified by Ting et al. (2018b; roughly 2×10^5 stars), which exhibit a narrow range of stellar parameters and which have very precise photometric distances, this feature disappears. The shape and morphology of flaring in the elements are preserved when examining the red clump stars only. Finally, we note that both $[\text{Ba}/\text{Fe}]$ and $[\text{O}/\text{Fe}]$ appear to be asymmetrically distributed about the Galaxy’s midplane. This asymmetry in the mean abundance value around the midplane persists in maps of the (R, z) plane made with only red clump stars, suggesting that they are not related to T_{eff} -dependent systematics. As seen in Figure 13, this feature does not correlate clearly with T_{eff} or $\log(g)$, nor does it trace extinction as traced by dust maps, or mean S/N of the stars. We do not rule out the possibility that the midplane asymmetry seen in these elements is caused by selection effects, particularly in light of the fact that these asymmetrical features are stretched along lines of sight.

Figure 14 shows mean abundance maps in the (X, Y) plane for kinematic thin-disk stars ($J_z < 30 \text{ kpc km s}^{-1}$), as well as mean T_{eff} and A_V maps, for comparison. We highlight the apparent azimuthal structure in $[\text{Mn}/\text{Fe}]$ and $[\text{O}/\text{Fe}]$, which is not easily explained by spurious correlation with T_{eff} , A_V , S/N, z , or J_z . These are two abundances for which our inferred values have lower relative uncertainty (Figure 9). Again, we note that a complete treatment of these data would involve explicit modeling of the LAMOST selection function. Note that the sensitivity of $[\text{Ba}/\text{Fe}]$ to T_{eff} is clearly visible. Like the “cone” in the (R, z) plane, correlation of $[\text{Ba}/\text{Fe}]$ with heliocentric distance disappears in maps including only red clump stars. The patterns in these maps along lines of sight are likely of an observational origin but are not easily explained by a single confounding factor. They do not trace mean height, extinction, metallicity, T_{eff} , or $\log(g)$.

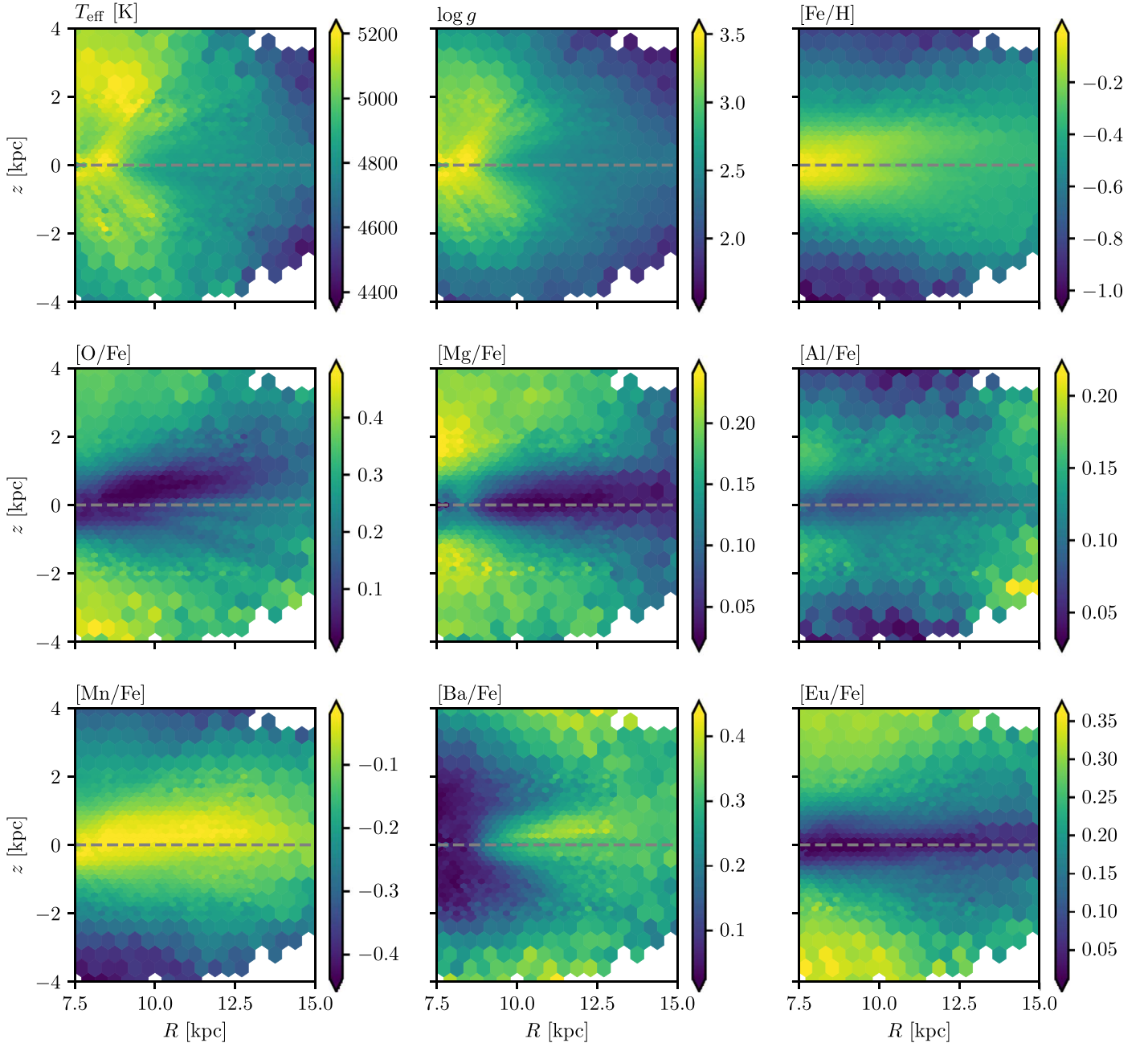


Figure 13. (R, z) plane colored by mean label value for nine labels of our 800,000 giant stars, summed over all ϕ . The flaring of the disk can be seen in [Eu/Fe], [Mg/Fe], and [Mn/Fe].

Azimuthal trends in abundance are known to exist in Galactic gas and are often attributed to spiral structure (e.g., Wenger et al. 2019). Variations in the height of the midplane in combination with LAMOST’s selection function could give rise to azimuthal abundance gradients, but it is not clear why this would be manifest in some abundances and not others unless due to abundance–age correlations, which does not appear to be the case here. Additionally, there is no correlation between the strength of vertical (Figure 13) and azimuthal (Figure 14) gradients, which would be expected if the azimuthal trends were due to midplane variations.

Figure 15 shows mean abundance maps of LAMOST giants for the thin disk ($J_z < 30 \text{ kpc km s}^{-1}$) in the (R, v_ϕ) plane. By using LAMOST RVs, we are able to probe farther out into the

disk than with the Gaia DR2 RVS sample. In this plane a particularly prominent feature are the “ridges” first reported by Kawata et al. (2018). A number of interpretations have been given for the origin of these ridges, including perturbations introduced by spirals, the bar, an external perturber, or a combination of these (e.g., Antoja et al. 2018; Bland-Hawthorn et al. 2019; Fragkoudi et al. 2019, 2020; Khanna et al. 2019; Laporte et al. 2019). Of particular interest is the longest ridge (outlined by a dashed line). A. Wheeler et al. (2019, in preparation) will discuss its dynamical origin. Of our abundances, the ridge is most visible in the [O/Fe] and [Mn/Fe]. These are two elements that display the clearest azimuthal abundance gradients, and for which our inferred abundances have the lowest relative uncertainty (see Figure 9).

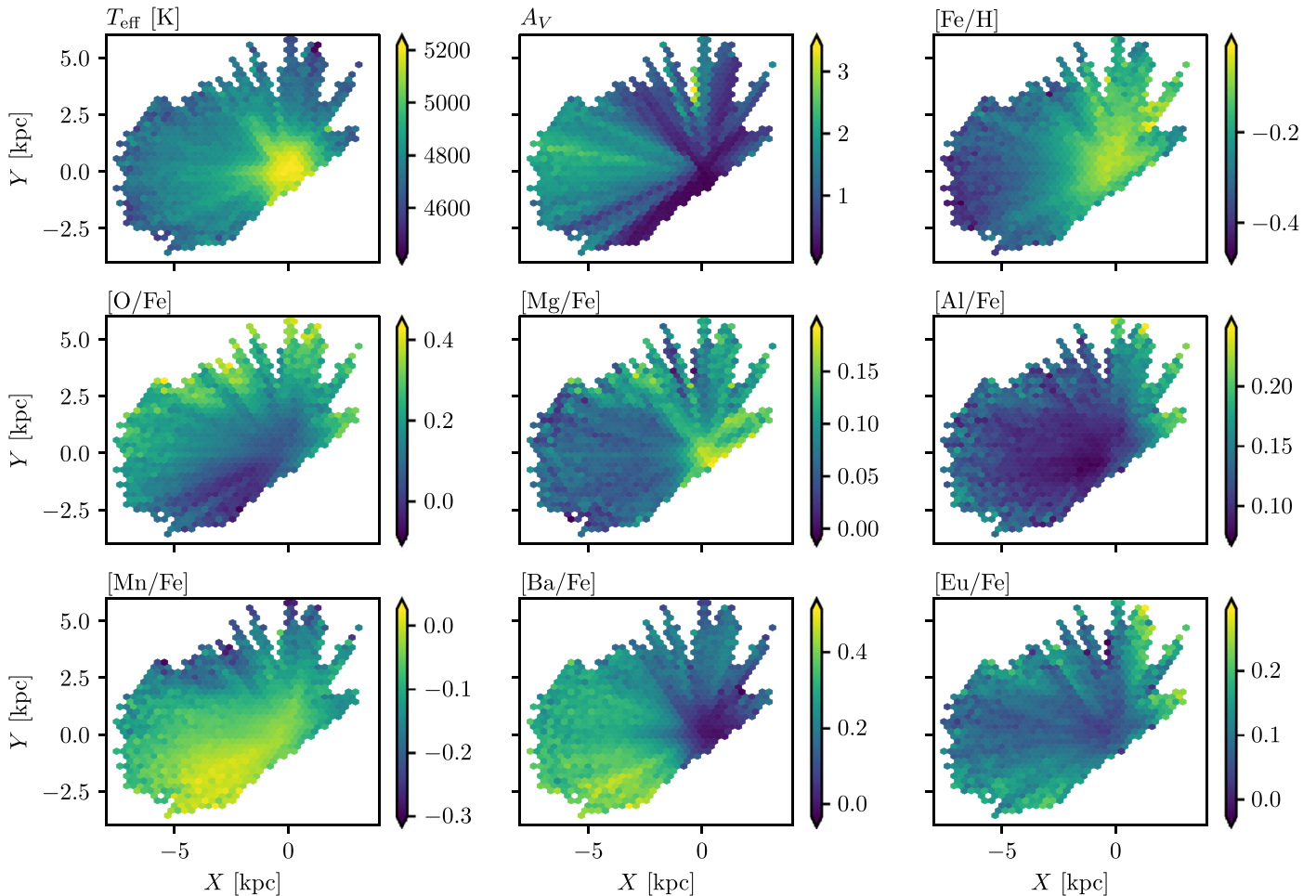


Figure 14. Mean abundances of LAMOST giants in the thin disk ($J_z < 30$ kpc km s $^{-1}$), mapped in the (X, Y) plane. T_{eff} and A_V are also mapped for comparison.

5.4. The Disk–Halo Transition Seen in Chemistry

The distributions of the neutron capture elements, $[\text{Ba}/\text{Fe}]$ and $[\text{Eu}/\text{Fe}]$, versus $[\text{Fe}/\text{H}]$, colored by v_ϕ , are plotted in spatial bins in Figures 16 and 17. Because of the T_{eff} -dependent systematics in $[\text{Ba}/\text{Fe}]$, we have only plotted stars with $4800 \text{ K} < T_{\text{eff}} < 5000 \text{ K}$ in Figure 16. Using other temperature ranges does not qualitatively change the plot, but not restricting T_{eff} yields higher dispersion in $[\text{Ba}/\text{Fe}]$. The azimuthal velocity, v_ϕ , allows us to clearly distinguish between the disk and halo populations at the scale heights (and vertical actions, J_z) where both are present (primarily the center row in Figures 16 and 17), illuminating the chemical differences between them. Disk stars are prograde across R and concentrated to low z , with most disk stars having $v_\phi \gtrsim 100$ km s $^{-1}$. There are fewer metal-poor disk stars as R increases, with a narrower, more metal-rich distribution at larger R , seen across the smallest z range. Halo stars are seen at larger z and are characterized by their more isotropic, eccentric orbits. At $11 \text{ kpc} < R < 13 \text{ kpc}$, most halo stars have $v_\phi \lesssim 200$ km s $^{-1}$ with a distribution of $v_\phi = 80 \pm 70$ km s $^{-1}$. The halo stars also appear to have increasingly negative velocities in the inner Galaxy. At our intermediate height from the plane, $2 \text{ kpc} < z < 4 \text{ kpc}$, the metal-poor stars ($[\text{Fe}/\text{H}] < -1.0$) are predominantly retrograde at our smallest R range, $3 \text{ kpc} < R < 5 \text{ kpc}$. Cutoffs of $J_R \approx 100$ km s $^{-1}$ kpc and $J_\phi \approx 1500$ km s $^{-1}$ kpc also clearly distinguish between disk and halo stars at large R . These

populations are not as dramatically distinguished at small R because distance errors propagate to larger uncertainties in v_ϕ (see Appendix D).

The distribution of (kinematic) halo stars in the $([\text{Ba}/\text{Fe}], [\text{Fe}/\text{H}])$ plane has a transition at $[\text{Fe}/\text{H}] \approx -1$ (most clearly seen in the middle row of Figure 16, $2 \text{ kpc} < |z| < 4 \text{ kpc}$). This metallicity corresponds to the transition between the disk and halo, as well as the approximate boundary between the accreted and (at least one component of the) in situ halo (Bonaca et al. (2017), called “the splash” in Belokurov et al. (2020) and the “heated thick disk” by Di Matteo et al. (2019)). At least for barium, the abundance planes at $4 \text{ kpc} < |z| < 6 \text{ kpc}$ suggest an overlap in the chemical plane of different sequences, perhaps associated with the accreted and in situ halo. Both $[\text{Eu}/\text{Fe}]$ and $[\text{Ba}/\text{Fe}]$ have larger dispersion at high $[\text{Fe}/\text{H}]$, but the sequence of europium abundances varies less across z .

6. Discussion and Conclusions

We have trained a data-driven model (*The Cannon*) to estimate detailed abundances from low-resolution LAMOST spectra, delivering up to seven abundances for 3.9×10^6 stars to a precision of 0.05–0.23 dex. A total of 2.9×10^6 of these are dwarf stars, for which we infer labels with 0.05–0.23 dex precision. A total of 8.8×10^5 are red giants for which we infer

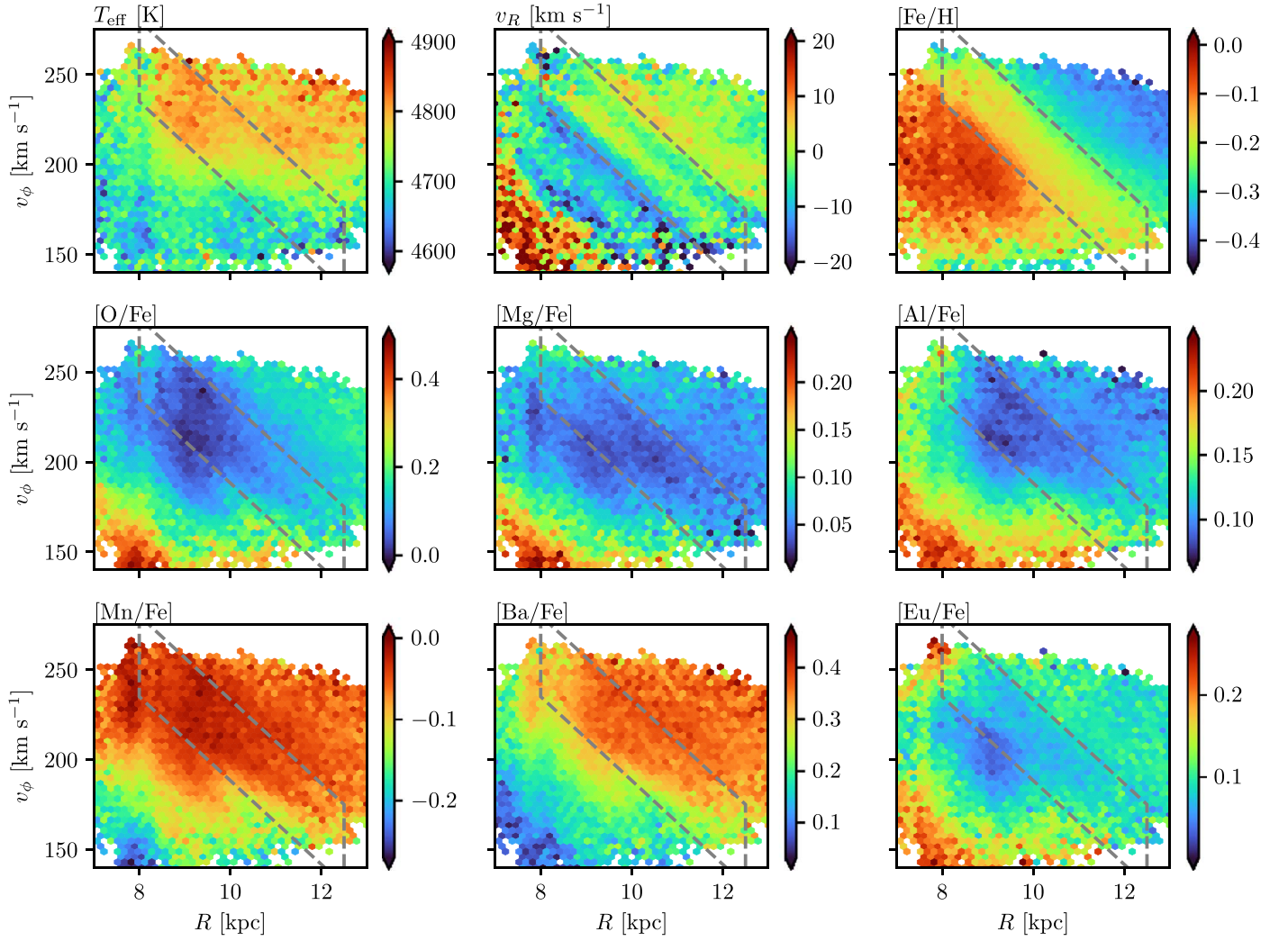


Figure 15. Mean abundance maps of thin-disk ($J_z < 30 \text{ kpc km s}^{-1}$) LAMOST giants in the (R, v_ϕ) plane. The dashed box outlines the longest ridge of increased stellar number density. We plot only stars with $\log(g) < 3$ to minimize contamination from dwarfs, whose abundances are generally on a different scale and have T_{eff} -dependent systematic trends, but a vertical feature is still visible at the solar radius, $R = 8 \text{ kpc}$, presumably induced by the selection function.

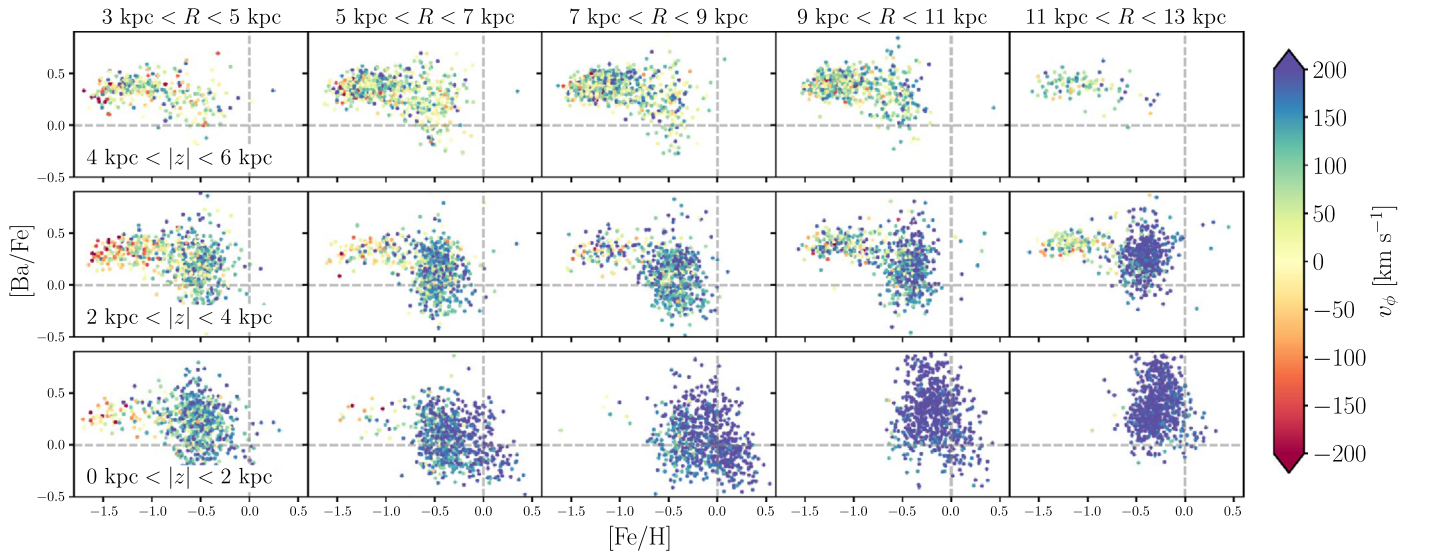


Figure 16. $([\text{Ba}/\text{Fe}]-[\text{Fe}/\text{H}])$ plane, colored by azimuthal velocity, v_ϕ , and plotted in spatial bins in the Galaxy, with (up to) 700 randomly selected stars plotted in each bin. Because of the T_{eff} -dependent systematics in our inferred $[\text{Ba}/\text{Fe}]$ values, we have only plotted stars with $4800 \text{ K} < T_{\text{eff}} < 5000 \text{ K}$. With increasing $|z|$, halo stars (as distinguished by their lower ϕ -velocities) become more dominant.

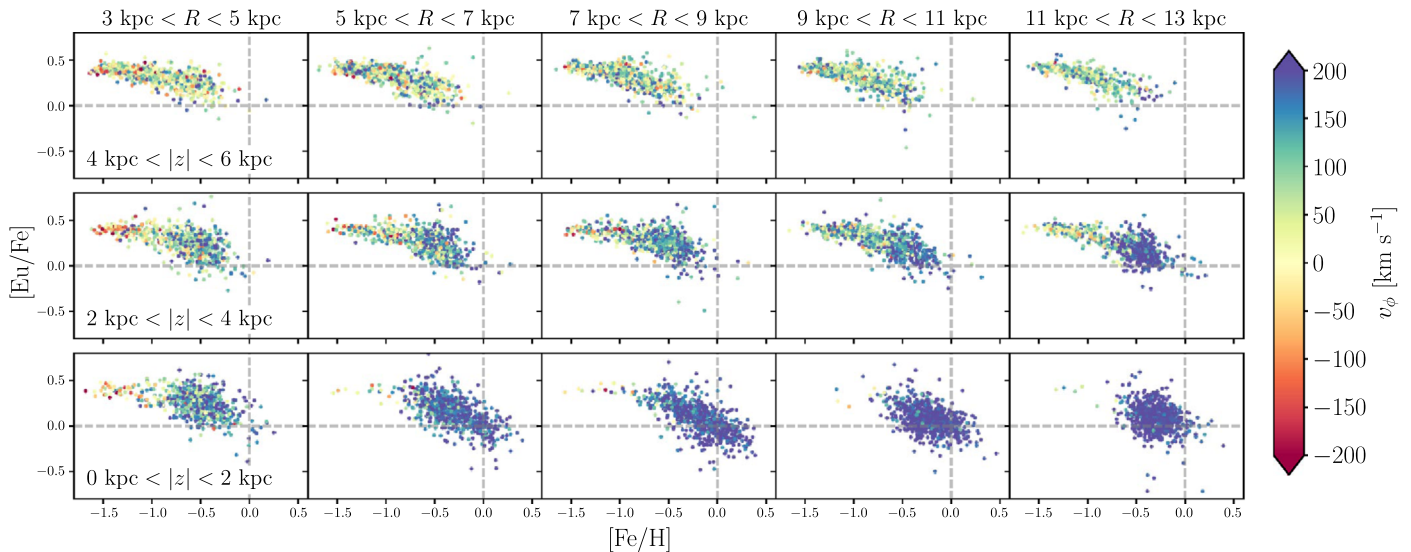


Figure 17. Same as Figure 16, with $[\text{Eu}/\text{Fe}]$ in place of $[\text{Ba}/\text{Fe}]$ and with stars chosen without restriction on T_{eff} .

abundances with 0.07–0.22 dex precision. Our best-fit model spectra are easily reproducible using our catalog, implementation of *The Cannon*, and model coefficients,¹⁵ which are available online. We used the red giants to examine the spatial distribution of abundances in the disk and halo and the dwarf stars to investigate the chemical similarity of wide binaries.

Our analysis of the chemical similarity of dwarf stars in wide binaries compared to field stars showed that these stars are from a common birth site and enabled us to quantify the additional resolving or discriminating power in the vector of our derived abundances beyond an overall metallicity.

Using the red giants, we first mapped the profile of the disk in the (R, z) plane in the elements O, Eu, Mg, Al, Mn, and Ba. These maps show the flaring of the disk and the distinction in abundances between the halo population at high latitudes and the disk. Second, we examined face-on projections across the disk in this set of abundances. These projections hint at some nonaxisymmetric patterns in the abundances. Indeed, the Gaia mission has revealed numerous dynamical deviations from axisymmetry in the disk and perturbations in the solar neighborhood (Antoja et al. 2018; Sellwood et al. 2019; Trick et al. 2019). Third, we constructed mean abundance maps in the (R, v_{ϕ}) plane and discuss the chemical signature of the high-density ridges in this plane. Finally, we investigated the abundance planes of $[\text{Ba}/\text{Fe}]$ – $[\text{Fe}/\text{H}]$ and $[\text{Eu}/\text{Fe}]$ – $[\text{Fe}/\text{H}]$ across (R, z) , making similar maps to Hayden et al. (2015), but with the neutron capture abundances. These maps showed the disk and halo trends across $[\text{Fe}/\text{H}]$ at all (R, z) . These different trends might be used to separate any in situ halo from heated disk stars, from an accreted halo. As the set of abundances we deliver give higher discriminating power to identify chemically similar stars compared to $[\text{Fe}/\text{H}]$ alone, we expect that the multiple families of abundances will be useful for studies of the plethora of chemodynamical substructure in the Milky Way halo (see, e.g., Antoja et al. 2018; Di Matteo et al. 2019; Helmi et al. 2018; Myeong et al. 2019; Belokurov et al. 2020).

We derive abundances with diverse nucleosynthetic channels and are demonstrably uncovering some of the breadth of chemical information in the Milky Way. However, a number

of caveats are discussed in Section 5.1, and we further detail some of these here.

In contrast to Ho et al. (2017a, 2017b), we find that our CV results do not vary strongly with S/N. This indicates that our precision is limited by that of reference labels themselves, and, if improved, we would obtain higher-precision results for our test objects that scale as expected with S/N.

Because our model is in some cases not inferring abundances from the corresponding lines themselves, it may not be robust to stars with properties or enrichment histories not represented in the training set. This means that while stars that are highly enriched or depleted in an element may not have their abundances accurately inferred, the best-fit model should have large residuals in regions of its known lines. Casey et al. (2019) used this effect to identify stars that are unusually rich in lithium, but this approach could be extended to all elements with strong lines in the LAMOST wavelength range. In particular, it is challenging to measure r -process abundances from r -process absorption features even from extremely high quality, high resolution spectra, and GALAH uses only two relatively unblended absorption regions for their $[\text{Eu}/\text{Fe}]$ measurement (Table C1). It raises questions about stellar spectra that we are inferring $[\text{Eu}/\text{Fe}]$ (albeit noisily) from relatively low S/N, low resolution spectra, as confirmed by CV, and that the $[\text{Eu}/\text{Fe}]$ distribution across $[\text{Fe}/\text{H}]$ mirrors that of boutique studies (e.g., Bensby et al. 2005). The physical origin of the significant correlations between absorption features of nominally different nucleosynthetic families (Feeney et al. 2019) is not clear but is presumably caused by a combination of the inherent correlation induced by element-production mechanisms, shared chemical enrichment history, and stellar physics. In other words, the chemical manifold on which the majority of stars lie is not well known. Of significant interest is most likely those stars where we cannot well match the spectra with our data-driven model, which is by far the minority of stars in LAMOST.

The large number of low- and medium-resolution spectra available now (RAVE and SEGUE, in addition to LAMOST) and coming in the near future (e.g., WEAVE, Dalton et al. 2012, MOONs, Cirasuolo et al. 2014; 4MOST, de Jong et al. 2019 in their lower-resolution modes; DESI, DESI Collaboration et al. 2016; Sloan V, Kollmeier et al. 2017; Gaia, Gaia Collaboration et al. 2016) makes honing our ability to learn from these data a

¹⁵ See doi:10.7910/DVN/5VWKMC.

fruitful endeavor. We also discussed future improvements to our methodology, especially the possibility of using open clusters to reduce the effect of systematic trends with stellar parameters in inferred abundances. Other promising methodological directions include using more robust inference for model parameters and labels, perhaps allowing more rigorous error estimation, and allowing missing labels in the training set, which would enable us to use training data from multiple surveys.

The authors thank Kathryn Johnston, James Applegate, David Helfand, Tomer Yavetz, Klemen Čotar, Francesca Fragkoudi, and Matthew Abruzzo for useful discussion and notes. We thank Matthias Steinmetz for his constructive comments that have improved the paper.

A.J.W. is supported by the National Science Foundation Graduate Research Fellowship under grant No. 1644869.

M.K.N. is in part supported by a Sloan Research Fellowship. We thank and acknowledge the Kavli Institute for Theoretical Physics at the University of California, Santa Barbara, and in particular the Gaia19 workshop. This work was also in part inspired during the Aspen Center for Physics “Dynamics of the Milky Way System in the Era of Gaia” workshop, which is supported by National Science Foundation grant PHY-1607611.

S.B. acknowledges funds from the Alexander von Humboldt Foundation in the framework of the Sofja Kovalevskaja Award endowed by the Federal Ministry of Education and Research. This research has been supported by the Australian Research Council (grants DP150100250 and DP160103747). Parts of this research were supported by the Australian Research Council (ARC) Centre of Excellence for All Sky Astrophysics in 3 Dimensions (ASTRO 3D), through project No. CE170100013.

J.B.-H. is funded by an ARC Laureate Fellowship.

D.B.Z. and J.D.S. acknowledge the support of the Australian Research Council through Discovery Project grant DP180101791.

T.Z. acknowledges the financial support of the Slovenian Research Agency (core funding P1-0188).

This research was supported in part by the National Science Foundation under grant No. NSF PHY-1748958.

Guoshoujing Telescope (the Large Sky Area Multi-Object Fiber Spectroscopic Telescope LAMOST) is a National Major Scientific Project built by the Chinese Academy of Sciences. Funding for the project has been provided by the National Development and Reform Commission. LAMOST is operated and managed by the National Astronomical Observatories, Chinese Academy of Sciences.

We acknowledge computing resources from Columbia University’s Shared Research Computing Facility project, which is supported by NIH Research Facility Improvement grant 1G20RR030893-01, and associated funds from the New York State Empire State Development, Division of Science Technology and Innovation (NYSTAR) contract C090171, both awarded 2010 April 15.

This work has made use of data from the European Space Agency (ESA) mission Gaia (<https://www.cosmos.esa.int/gaia>), processed by the Gaia Data Processing and Analysis Consortium (DPAC, <https://www.cosmos.esa.int/web/gaia/dpac/consortium>). Funding for the DPAC has been provided by national institutions, in particular the institutions participating in the Gaia Multilateral Agreement.

This publication makes use of data products from the Wide-field Infrared Survey Explorer, which is a joint project of the University of California, Los Angeles, and the Jet Propulsion Laboratory/California Institute of Technology, and NEOWISE, which is a project of the Jet Propulsion Laboratory/California Institute of Technology. *WISE* and *NEOWISE* are funded by the National Aeronautics and Space Administration.

Software: Optim.jl (Mogensen & Riseth 2018), Matplotlib (Hunter 2007), galpy (Bovy 2015).

Appendix A Linear Coefficients

Figures A1 and A2 show the linear coefficients of our models as a function of wavelength.

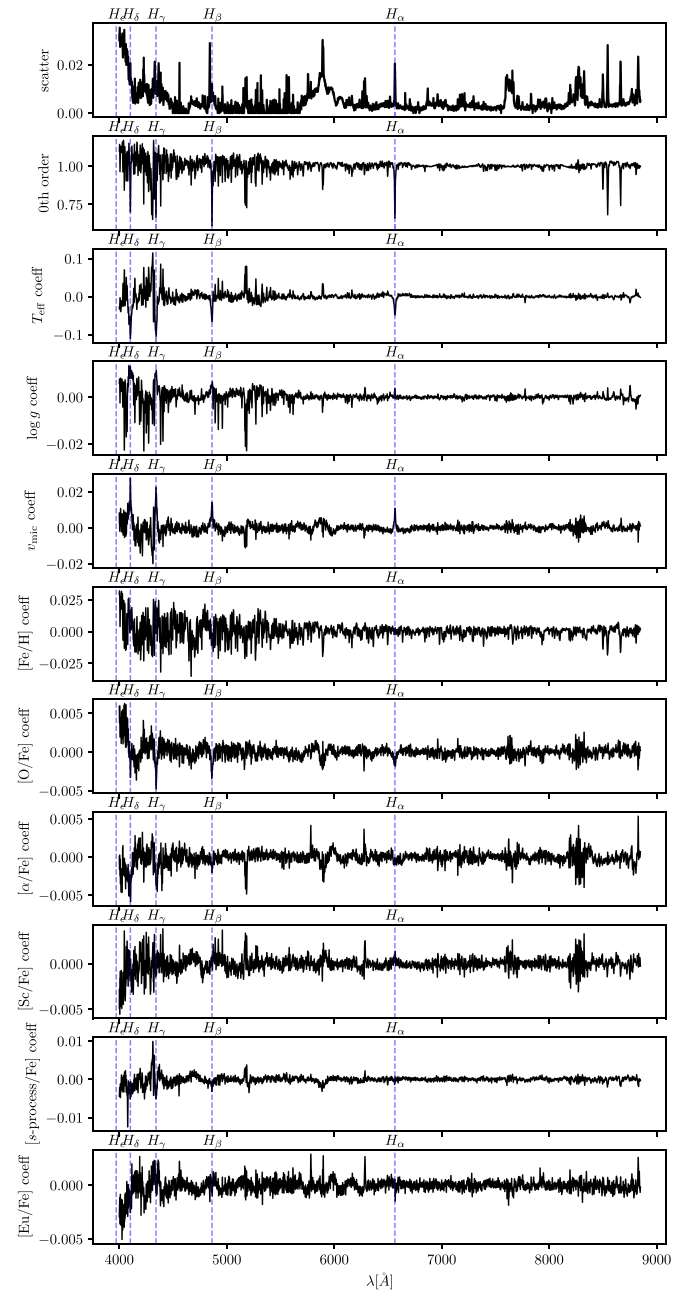


Figure A1. Linear coefficients for the dwarf model, omitting high-uncertainty pixels with $\lambda < 4000 \text{ \AA}$.

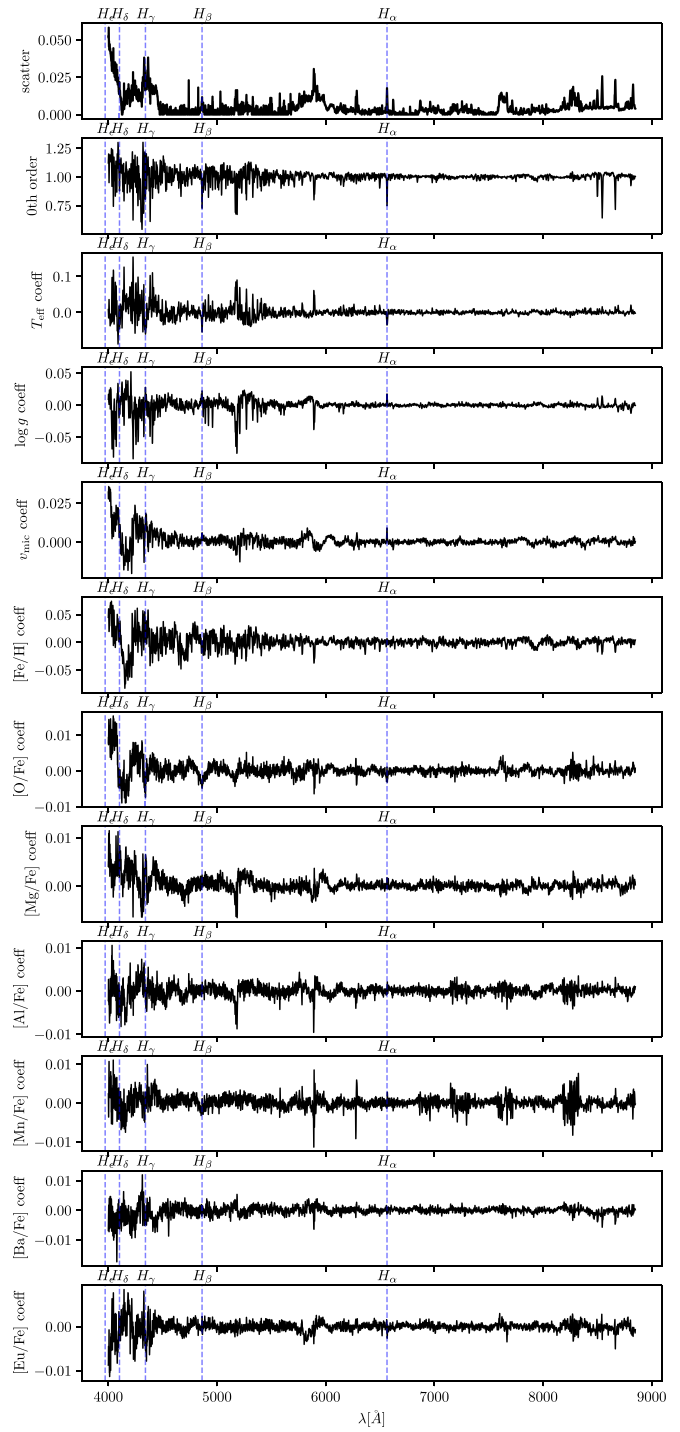


Figure A2. Same as Figure A1, but for our giant model.

Appendix B Radial Velocity Precision

Figure B1 shows reported RV error for stars in our catalog, as measured by Gaia and LAMOST.

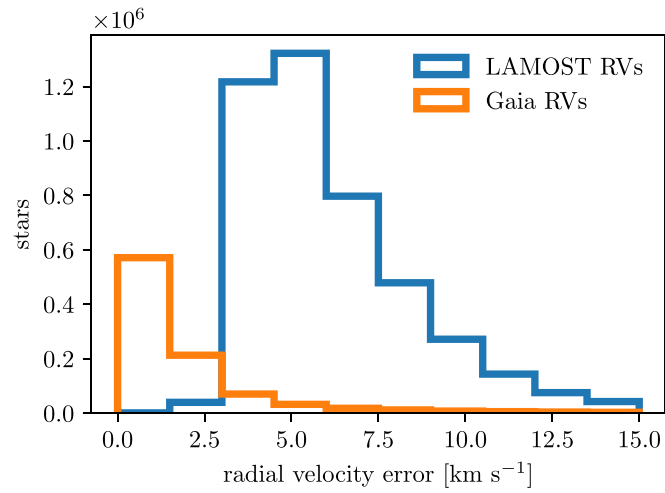


Figure B1. Reported RV precision of stars in our catalog from Gaia and LAMOST. While the LAMOST precision is worse, Gaia only measured RVs for approximately one-fifth of our catalog.

Appendix C GALAH Windows

Table C1 lists the GALAH line windows for each estimate element. We used these windows to calculate per-element χ^2 values for GALAH spectra to eliminate spurious measurements from our training set.

Table C1
GALAH Line Windows for Each Element

Element	Windows (Å)
Al	(6695.78, 6696.17), (6698.41, 6698.92), (7834.95, 7835.47), (7835.84, 7836.43)
Ba	(5853.53, 5853.86), (6496.68, 6497.19)
Ca	(5857.22, 5857.60), (5867.28, 5867.72), (6493.48, 6493.99), (6499.37, 6499.94), (6508.52, 6509.03)
Co	(6632.23, 6632.81), (7712.41, 7713.07), (7837.76, 7838.50)
Cr	(4775.03, 4775.21), (4789.20, 4789.47), (4800.83, 4801.20), (4847.98, 4848.31), (5702.12, 5702.50), (5719.50, 5719.99), (5787.64, 5788.14), (5844.40, 5844.79), (6629.80, 6630.25)
Cu	(5781.92, 5782.42)
Eu	(5818.61, 5818.99), (6644.97, 6645.29)
K	(7698.57, 7699.31)
La	(4716.29, 4716.61), (4748.62, 4748.85), (4803.92, 4804.24), (5805.52, 5805.96)
Li	(6707.37, 6708.26)
Mg	(4729.90, 4730.22), (5710.86, 5711.30)
Mn	(4739.01, 4739.29), (4761.37, 4761.64), (4765.69, 4766.06), (4783.17, 4783.58)
Na	(4751.71, 4751.94), (5682.54, 5682.92), (5687.93, 5688.37)
Ni	(5748.21, 5748.59), (5846.82, 5847.21), (6482.60, 6483.05), (6532.58, 6533.10), (6586.02, 6586.47), (6643.37, 6643.94), (7713.89, 7714.48), (7788.48, 7789.29)
O	(7771.53, 7772.27), (7773.75, 7774.57), (7775.08, 7775.75)
Sc	(4743.56, 4743.98), (4752.99, 4753.41), (5657.68, 5658.12), (5666.92, 5667.30), (5671.59, 5672.09), (5684.02, 5684.30), (5686.72, 5687.21), (5717.02, 5717.52), (5723.90, 5724.28), (6604.39, 6604.97)
Si	(5665.21, 5665.82), (5690.18, 5690.68), (5700.91, 5701.29), (5792.70, 5793.31)
Ti	(4719.32, 4719.60), (4757.96, 4758.28), (4759.07, 4759.48), (4764.40, 4764.82), (4778.06, 4778.43), (4781.56, 4781.93), (4797.84, 4798.12), (4798.35, 4798.63), (4801.80, 4802.21), (4820.11, 4820.66), (4849.04, 4849.41), (4865.28, 4865.83), (4873.88, 4874.20), (5689.25, 5689.80), (5716.25, 5716.80), (5720.27, 5720.65), (5739.24, 5739.68), (5866.02, 5866.79), (6598.89, 6599.53), (6716.52, 6716.90), (7852.19, 7853.01)
V	(4746.51, 4746.78), (4784.32, 4784.60), (4796.74, 4796.97), (4831.52, 4831.75), (4875.26, 4875.72), (5657.07, 5657.68), (5668.13, 5668.62), (5670.60, 5671.10), (5702.78, 5703.88), (5725.27, 5725.82), (5726.87, 5727.36), (5727.42, 5727.97), (5730.99, 5731.49), (5736.82, 5737.26), (5743.20, 5743.70), (6531.18, 6531.62)
Y	(4854.79, 4855.02), (4883.54, 4883.82), (5662.74, 5663.18), (5728.74, 5729.01)
Zn	(4721.99, 4722.27), (4810.36, 4810.63)

Appendix D

Action and Azimuthal Velocity Uncertainty

Figure D1 shows the median values and errors of the three actions and azimuthal velocity as a function of Galactocentric radius. J_R is particularly uncertain, and extremely so for stars interior to the Sun.

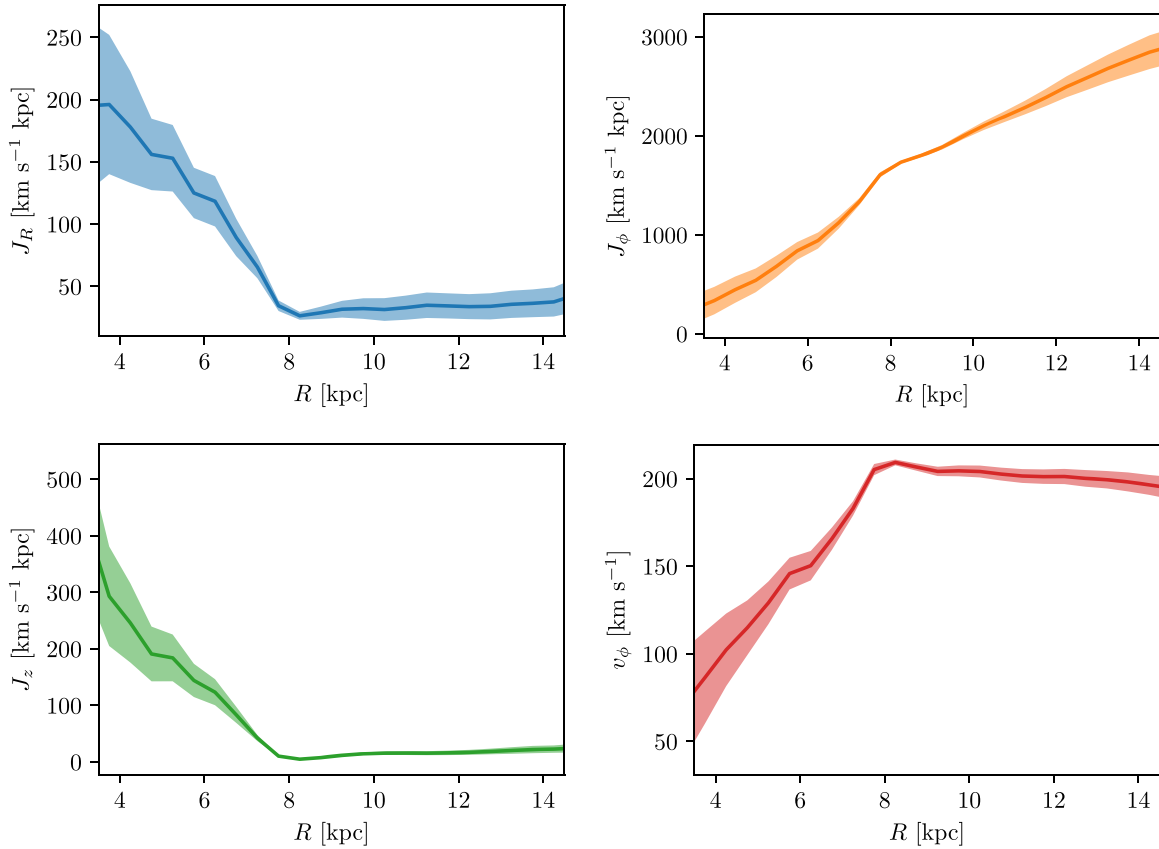




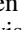








Figure D1. Median values and uncertainties of the three actions and azimuthal velocity as a function of Galactocentric radius, R . Note that the error bars here do not show scatter, but median uncertainty.

ORCID iDs

Adam Wheeler  <https://orcid.org/0000-0001-7339-5136>
 Melissa Ness  <https://orcid.org/0000-0001-5082-6693>
 Sven Buder  <https://orcid.org/0000-0002-4031-8553>
 Joss Bland-Hawthorn  <https://orcid.org/0000-0001-7516-4016>
 Michael Hayden  <https://orcid.org/0000-0001-7294-9766>
 Geraint F. Lewis  <https://orcid.org/0000-0003-3081-9319>
 Sarah Martell  <https://orcid.org/0000-0002-3430-4163>
 Sanjib Sharma  <https://orcid.org/0000-0002-0920-809X>
 Jeffrey D. Simpson  <https://orcid.org/0000-0002-8165-2507>
 D. B. Zucker  <https://orcid.org/0000-0003-1124-8477>
 Tomaž Zwitter  <https://orcid.org/0000-0002-2325-8763>

References

- Anders, F., Khalatyan, A., Chiappini, C., et al. 2019, *A&A*, **A94**
 Andrews, J. J., Anguiano, B., Chanamé, J., et al. 2019, *ApJ*, **871**, 42
 Andrews, J. J., Chanamé, J., & Agüeros, M. A. 2018, *MNRAS*, **473**, 5393
 Antoja, T., Helmi, A., Romero-Gomez, M., et al. 2018, *Natur*, **561**, 360
 Armandroff, T. E., & Zinn, R. 1988, *AJ*, **96**, 92
 Arnould, M., Goriely, S., & Takahashi, K. 2007, *PhR*, **450**, 97
 Bailer-Jones, C. A. L., Rybizki, J., Fousneau, M., Mantelet, G., & Andrae, R. 2018, *AJ*, **156**, 58
 Bedell, M., Bean, J. L., Meléndez, J., et al. 2018, *ApJ*, **865**, 68
 Belokurov, V., Sanders, J. L., Fattahi, A., et al. 2020, *MNRAS*, **494**, 3880
 Bensby, T., Feltzing, S., Lundström, I., & Ilyin, I. 2005, *A&A*, **433**, 185
 Bensby, T., Feltzing, S., & Oey, M. S. 2014, *A&A*, **562**, A71
 Binney, J. 2012, *MNRAS*, **426**, 1324
 Birky, J., Hogg, D. W., Mann, A. W., & Burgasser, A. 2020, *ApJ*, **892**, 31
 Blancato, K., Ness, M., Johnston, K. V., Rybizki, J., & Bedell, M. 2019, *ApJ*, **883**, 34
 Bland-Hawthorn, J., & Gerhard, O. 2016, *ARA&A*, **54**, 529
 Bland-Hawthorn, J., Sharma, S., Tepper-Garcia, T., et al. 2019, *MNRAS*, **486**, 1167
 Bonaca, A., Conroy, C., Wetzel, A., Hopkins, P. F., & Keres, D. 2017, *ApJ*, **845**, 101
 Bovy, J. 2015, *ApJS*, **216**, 29
 Bovy, J., & Rix, H.-W. 2013, *ApJ*, **779**, 115
 Buder, S., Asplund, M., Duong, L., et al. 2018, *MNRAS*, **478**, 4513
 Buder, S., Lind, K., Ness, M. K., et al. 2019, *A&A*, **624**, A19
 Cantat-Gaudin, T., Jordi, C., Vallenari, A., et al. 2018, *A&A*, **618**, A93
 Casey, A. R., Ho, A. Y. Q., Ness, M., et al. 2019, *ApJ*, **880**, 125
 Casey, A. R., Hogg, D. W., Ness, M., et al. 2016, arXiv:1603.03040
 Cerasuolo, M., Afonso, J., Carollo, M., et al. 2014, *Proc. SPIE*, **9147**, 91470N
 Côte, B., Fryer, C. L., Belczynski, K., et al. 2018, *ApJ*, **855**, 99
 Cunha, K., Smith, V. V., Hasselquist, S., et al. 2017, *ApJ*, **844**, 145
 Dalton, G., Trager, S. C., Abrams, D. C., et al. 2012, *Proc. SPIE*, **8446**, 84460P
 de Jong, R. S., Agertz, O., Berbel, A. A., et al. 2019, *Msngr*, **175**, 3
 De Silva, G. M., Freeman, K. C., Bland-Hawthorn, J., et al. 2015, *MNRAS*, **449**, 2604
 DESI Collaboration, Aghamousa, A., Aguilar, J., et al. 2016, arXiv:1611.00036
 Di Matteo, P., Haywood, M., Lehnert, M. D., et al. 2019, *A&A*, **632**, A4
 Dotter, A., Conroy, C., Cargile, P., & Asplund, M. 2017, *ApJ*, **840**, 99
 El-Badry, K., Rix, H.-W., Tian, H., Duchêne, G., & Moe, M. 2019, *MNRAS*, **489**, 5822
 Feeney, S. M., Wandelt, B. D., & Ness, M. K. 2019, arXiv:1912.09498
 Feuillet, D. K., Bovy, J., Holtzman, J., et al. 2018, *MNRAS*, **477**, 2326
 Feuillet, D. K., Frankel, N., Lind, K., et al. 2019, *MNRAS*, **489**, 1742
 Fragkoudi, F., Grand, R. J. J., Pakmor, R., et al. 2020, *MNRAS*, **494**, 5936
 Fragkoudi, F., Katz, D., Trick, W., et al. 2019, *MNRAS*, **488**, 3324
 Freeman, K., & Bland-Hawthorn, J. 2002, *ARA&A*, **40**, 487
 Gaia Collaboration, Babusiaux, C., van Leeuwen, F., et al. 2018, *A&A*, **616**, A10
 Gaia Collaboration, Prusti, T., de Bruijne, J. H. J., et al. 2016, *A&A*, **595**, A1
 Gao, X., Lind, K., Amarsi, A. M., et al. 2018, *MNRAS*, **481**, 2666
 García Pérez, A. E., Allende Prieto, C., Holtzman, J. A., et al. 2016, *AJ*, **151**, 144
 Gilmore, G., Randich, S., Asplund, M., et al. 2012, *Msngr*, **147**, 25
 Hansen, T. T., Holmbeck, E. M., Beers, T. C., et al. 2018, *ApJ*, **858**, 92
 Hasselquist, S., Shetrone, M., Cunha, K., et al. 2016, *ApJ*, **833**, 81
 Hawkins, K., Lucey, M., Ting, Y.-S., et al. 2020, *MNRAS*, **492**, 1164
 Hayden, M. R., Bovy, J., Holtzman, J. A., et al. 2015, *ApJ*, **808**, 132
 Helmi, A., Babusiaux, C., Koppelman, H. H., et al. 2018, *Natur*, **563**, 85
 Ho, A. Y. Q., Ness, M. K., Hogg, D. W., et al. 2017a, *ApJ*, **836**, 5
 Ho, A. Y. Q., Rix, H.-W., Ness, M. K., et al. 2017b, *ApJ*, **841**, 40
 Hogg, D. W., Eilers, A.-C., & Rix, H.-W. 2018, arXiv:1810.09468
 Holtzman, J. A., Hasselquist, S., Shetrone, M., et al. 2018, *AJ*, **156**, 125
 Hunter, J. D. 2007, *CSE*, **9**, 90
 Jurić, M., Ivezić, Ž., Brooks, A., et al. 2008, *ApJ*, **673**, 864
 Kamdar, H., Conroy, C., Ting, Y.-S., et al. 2019, *ApJL*, **884**, L42
 Kawata, D., Baba, J., Ciucă, I., et al. 2018, *MNRAS: Lett.*, **479**, L108
 Kemp, A. J., Casey, A. R., Miles, M. T., et al. 2018, *MNRAS*, **480**, 1384
 Khanna, S., Sharma, S., Tepper-Garcia, T., et al. 2019, *MNRAS*, **489**, 4962
 Kollmeier, J. A., Zasowski, G., Rix, H.-W., et al. 2017, arXiv:1711.03234
 Krumholz, M. R., McKee, C. F., & Bland-Hawthorn, J. 2019, *ARA&A*, **57**, 227
 Laporte, C. F. P., Minchev, I., Johnston, K. V., & Gómez, F. A. 2019, *MNRAS*, **485**, 3134
 Lee, Y. S., Beers, T. C., Prieto, C. A., et al. 2011, *AJ*, **141**, 90
 Leung, H. W., & Bovy, J. 2019, *MNRAS*, **483**, 3255
 Li, J., Han, C., Xiang, M.-S., et al. 2016, *RAA*, **16**, 110
 Mainzer, A., Bauer, J., Grav, T., et al. 2011, *ApJ*, **731**, 53
 Majewski, S. R., Schiavon, R. P., Frinchaboy, P. M., et al. 2017, *AJ*, **154**, 94
 Majewski, S. R., Zasowski, G., & Nidever, D. L. 2011, *ApJ*, **739**, 25
 Martell, S., Sharma, S., Buder, S., et al. 2017, *MNRAS*, **465**, 3203
 Minchev, I., Anders, F., Recio-Blanco, A., et al. 2018, *MNRAS*, **481**, 1645
 Minchev, I., Chiappini, C., & Martig, M. 2014, *A&A*, **572**, A92
 Minchev, I., Famaey, B., Quillen, A. C., et al. 2012, *A&A*, **548**, A127
 Mogensen, P. K., & Riseth, A. N. 2018, *JOSS*, **3**, 615
 Myeong, G. C., Vasiliev, E., Iorio, G., Evans, N. W., & Belokurov, V. 2019, *MNRAS*, **488**, 1235
 Ness, M., Hogg, D. W., Rix, H. W., Ho, A. Y. Q., & Zasowski, G. 2015, *ApJ*, **808**, 16
 Ness, M., Hogg, D. W., Rix, H.-W., et al. 2016, *ApJ*, **823**, 114
 Ness, M., Rix, H.-W., Hogg, D. W., et al. 2018, *ApJ*, **853**, 198
 Ness, M. K., Johnston, K. V., Blancato, K., et al. 2019, *ApJ*, **883**, 177
 Newberg, H. J., Johnston, K. V., Blancato, K., et al. 2012, *RAA*, **12**, 735
 Nidever, D. L., Bovy, J., Bird, J. C., et al. 2014, *ApJ*, **796**, 38
 Norfolk, B. J., Casey, A. R., Karakas, A. I., et al. 2019, *MNRAS*, **490**, 2219
 Price-Jones, N., & Bovy, J. 2018, *MNRAS*, **475**, 1410
 Ramirez, I., Khanal, S., Lichon, S. J., et al. 2019, *MNRAS*, **490**, 2448
 Roškar, R., Debattista, V. P., Quinn, T. R., Stinson, G. S., & Wadsley, J. 2008, *ApJL*, **684**, L79
 Rybizki, J., Just, A., & Rix, H.-W. 2017, *A&A*, **605**, A59
 Sakari, C. M., Placco, V. M., Farrell, E. M., et al. 2018, *ApJ*, **868**, 110
 Sakari, C. M., Roederer, I. U., Placco, V. M., et al. 2019, *ApJ*, **874**, 148
 Schoenrich, R., & Binney, J. 2009, *MNRAS*, **399**, 1145
 Schönrich, R., & Weinberg, D. H. 2019, *MNRAS*, **487**, 580
 Sellwood, J. A., Trick, W., Carlberg, R., Coronado, J., & Rix, H.-W. 2019, *MNRAS*, **484**, 3154
 Siegel, D. M., Barnes, J., & Metzger, B. D. 2019, *Natur*, **569**, 241
 Silverman, B. W. 1986, *Density Estimation for Statistics and Data Analysis* (London: Chapman and Hall)
 Simpson, J. D., Martell, S. L., da Costa, G., et al. 2019, *MNRAS*, **482**, 5302
 Skrutskie, M. F., Cutri, R. M., Stiening, R., et al. 2006, *AJ*, **131**, 1163
 Souto, D., Prieto, C. A., Cunha, K., et al. 2019, *ApJ*, **874**, 97
 Spina, L., Mel'endez, J., Karakas, A. I., et al. 2018, *MNRAS*, **474**, 2580
 Steinmetz, M., Zwitter, T., Siebert, A., et al. 2006, *AJ*, **132**, 1645
 Ting, Y.-S., Conroy, C., Rix, H.-W., & Asplund, M. 2018a, *ApJ*, **860**, 159
 Ting, Y.-S., Conroy, C., Rix, H.-W., & Cargile, P. 2019, *ApJ*, **879**, 69
 Ting, Y.-S., Hawkins, K., & Rix, H.-W. 2018b, *ApJL*, **858**, L7
 Trick, W. H., Fragkoudi, F., Hunt, J. A. S., Mackereth, J. T., & White, S. D. M. 2019, arXiv:1906.04786
 Vásquez, S., Zoccali, M., Hill, V., et al. 2015, *A&A*, **580**, A121
 Weinberg, D. H., Holtzman, J. A., Hasselquist, S., et al. 2019, *ApJ*, **874**, 102
 Wenger, T. V., Bailer, D. S., Anderson, L. D., & Bania, T. M. 2019, *ApJ*, **887**, 114
 Wright, E. L., Eisenhardt, P. R. M., Mainzer, A. K., et al. 2010, *AJ*, **140**, 1868
 Xiang, M., Liu, X., Shi, J., et al. 2017, *MNRAS*, **464**, 3657
 Xiang, M., Ting, Y.-S., Rix, H.-W., et al. 2019, *ApJS*, **245**, 34
 Yanny, B., Rockosi, C., Newberg, H. J., et al. 2009, *AJ*, **137**, 4377
 Zhang, X., Zhao, G., Yang, C. Q., Wang, Q. X., & Zuo, W. B. 2019, *PASP*, **131**, 094202
 Zhao, G., Zhao, Y., Chu, Y., Jing, Y., & Deng, L. 2012, arXiv:1206.3569